A COMPARATIVE ANALYSIS OF WATER-EQUIVALENT PATH LENGTH OF TISSUE SAMPLES USING A FAST MONOLITHIC PROTON RADIOGRAPHY SYSTEM

A Thesis
Presented To
The Academic Faculty

By

Greg DeFillippo

In Partial Fulfillment
Of the Requirements for the Degree
Master of Science in Medical Physics

Georgia Institute of Technology

December 2020

A COMPARATIVE ANALYSIS OF WATER-EQUIVALENT PATH LENGTH OF TISSUE SAMPLES USING A FAST MONOLITHIC PROTON RADIOGRAPHY SYSTEM

Approved by:

Dr. C-K Chris Wang, Advisor

The George W. Woodruff School of Mechanical Engineering

Georgia Institute of Technology

Dr. Anna Erickson

The George W. Woodruff School of Mechanical Engineering

Georgia Institute of Technology

Mark Pankuch, Ph.D.

Department of Medical Physics

Northwestern Medicine Proton Center

Date Approved: Tuesday, November 24th, 2020

I can see! I… Can… FIGHT!

King Arthur Liebowitz, *The Fairly Odd Parents*

ACKNOWLEDGEMENTS

Mark Pankuch for his expert guidance and constant support

Dr. C-K Chris Wang for advising and administrative leadership

Virggie Lowe for taking the stress out of everything

Dr. Don De Jongh, Ethan DeJongh, Viktor Rykalin of ProtonVDA

Dr. James Welsh for his encouragement and understanding

John Edwards and Alan Camacho for their accommodation and support

Ming Gao for his infinite wisdom

Aidan Backus for help with MLP calculations

The Lads™ for emotional support and memes

and my parents, Gene and Sherry DeFillippo, for everything

TABLE OF CONTENTS

LIST OF TABLES

LIST OF FIGURES
not including appendices

LIST OF ABBREVIATIONS
in the order they appear

SOBP	Spread-Out Bragg Peak
NMPC	Northwestern Medicine Proton Center
RSP	Relative Stopping Power
CSDA	Continuous Slowing-Down Approximation
R80:	The range at which the distal falloff of the Bragg peak reaches 80% of the Bragg peak maximum
R90	As R80, but to 90% of the Bragg peak maximum
HU	Hounsfield Units
DECT	Dual-Energy Computed Tomography
PET	Positron Emission Tomography
DRR	Digitally Reconstructed Radiograph
pCT	Proton Computed Tomography
WEPL	Water-Equivalent Path Length
MCS	Multiple Coulomb Scattering
MLP	Most Likely Path
CAX	Central AXis
DROP	Diagonally-Relaxed Orthogonal Projections
CARP	Component-Averaged Row Projections
ART	Algebraic Reconstruction Technique
TVS	Total Variation Superiorization

NIU	Northern Illinois University
FNAL	Fermilab National Accelerator Laboratory
SSD	Silicon-Strip Detector
FPGA	Field-Programmable Gate Array
GEANT4	GEometry ANd Tracking, version 4
RMS	Root Mean Square
PBS	Pencil Beam Scanning
IBA	Ion Beam Applications
PM	Preventative Maintenance
ROI	Region of Interest

SUMMARY

Proton therapy has emerged over the past forty years as a clinically viable form of radiation oncology. With low entry dose, a rise to a sharp maximum, and a steep fall-off to zero dose after the "Bragg Peak", proton therapy has proven itself useful particularly with cancers in regions close to sensitive normal tissue. However, proton therapy treatment plans are still produced on x-ray CT scans. Due to fundamentally different natures of interaction, x-ray scans must undergo a conversion to translate Hounsfield Units (HU) to relative stopping power (RSP). This conversion can be inaccurate by up to 4%, and is currently the greatest cause of uncertainty in proton therapy. While there exist several ways around this, directly measuring RSP with proton imaging is the most accurate solution. ProtonVDA, in conjunction with Northern Illinois University, has produced a prototypical proton radiograph and CT scanner compatible with clinical pencil beam scanning (PBS) gantries. In this presentation, I demonstrate recent work on animal tissue samples using this scanner, including pork shoulder, pork ribs, and an in-tact pig head. A comparative analysis of RSP between x-ray CT and proton CT images of these samples is presented, along with sample pencil beam spots measured in the RayStation treatment program.

CHAPTER 1 - INTRODUCTION

1.1 Introduction to Proton Therapy

First suggested in 1946 by Dr. Robert R. Wilson, proton therapy has emerged in the past thirty years as a viable modality of radiation oncology (1). While originally put into practice in particle accelerator research facilities with a limited treatment scope, proton therapy is now used worldwide in medical centers to treat many different types of cancers. These dedicated medical centers utilize both large accelerators that supply protons for several treatment rooms as well as the newer single-room solutions. Currently there are 31 active proton centers across the US and many more overseas.

The primary benefit of proton therapy comes from its dose deposition along the beam axis which produces a relatively low entry dose, a rise to a sharp maximum, then a steep fall-off to zero dose. The proton peak dose is referred to as the Bragg peak. Figure 1 demonstrates a typical proton depth dose and demonstrates the sharp distal falloff to zero dose at the end of the proton's range. A lower entry dose and the drop to zero dose after the distal falloff is the primary benefit of proton therapy over photon therapy.

The depth in water at which the Bragg peak is deposited is dependent on the incident energy of the proton beam. By delivering

several proton beams with successive lower energies and successive lower intensities, the Bragg peak maximum dose can be "spread" over a desired depth range, creating a "Spread-Out Bragg Peak" (SOBP) seen in Figure 2. If the SOBP is spread across the entire depth of a target, the target will receive a uniform dose with lower entry dose than photons and zero dose past the distal end of the SOBP.

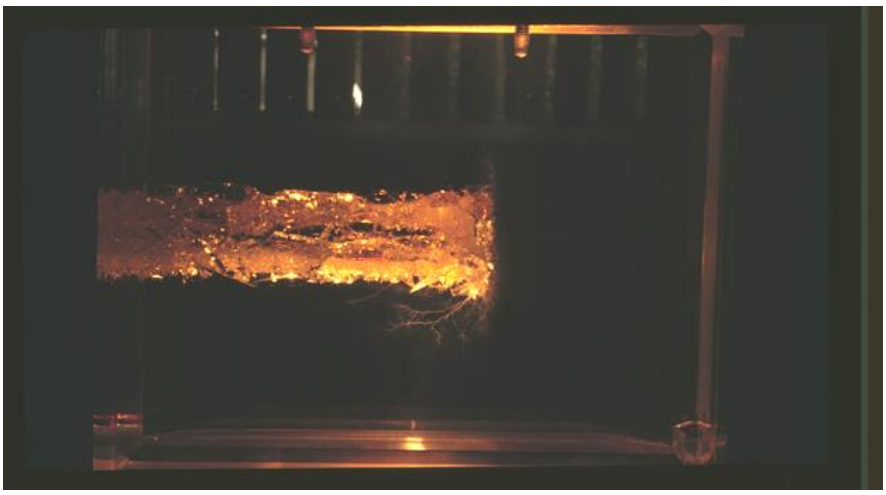

Fig. 1: A thin strip of scintillating plastic treated with a narrow proton beam from the left. Note the sharp distal falloff. Image from Northwestern Medicine Proton Center (NMPC).

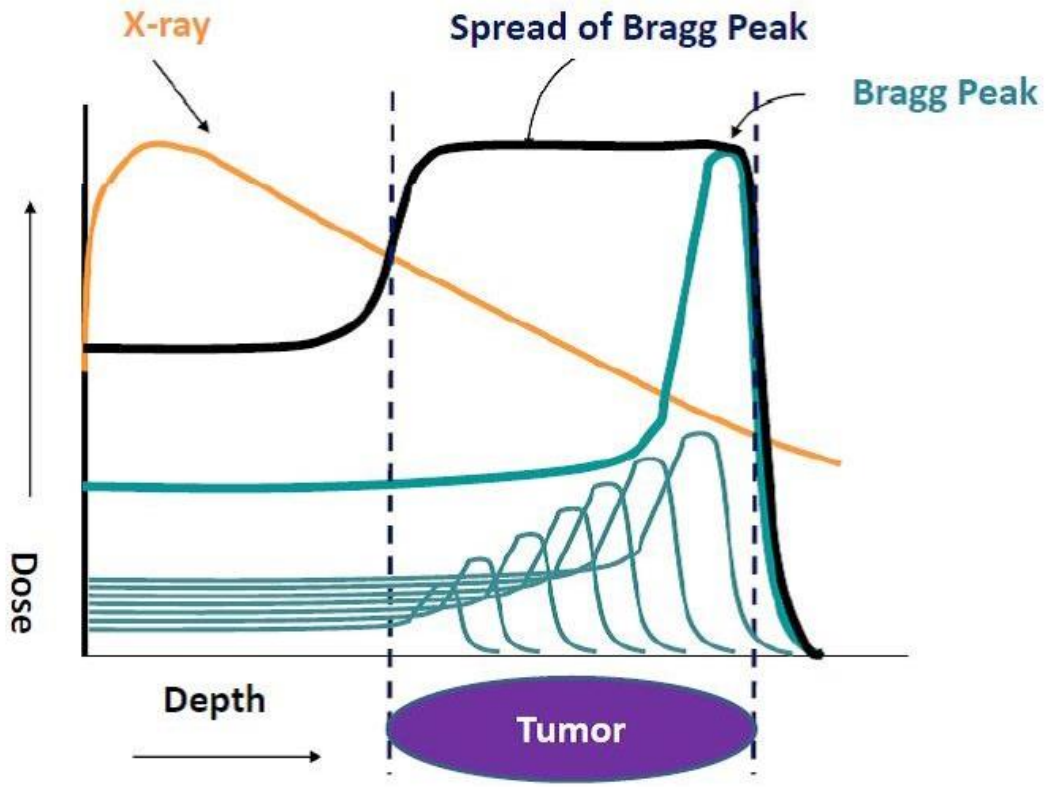

Fig. 2: A comparison of depth dose curves in uniform tissue. Pink: a 6MV photon beam. Red: a single monoenergetic 250 MeV proton beam. Blue: A range-modulated SOBP with a maximum energy of 250 MeV. Again, note the low entry dose, quick dose buildup, and sharp distal falloff of the proton profiles. (2).

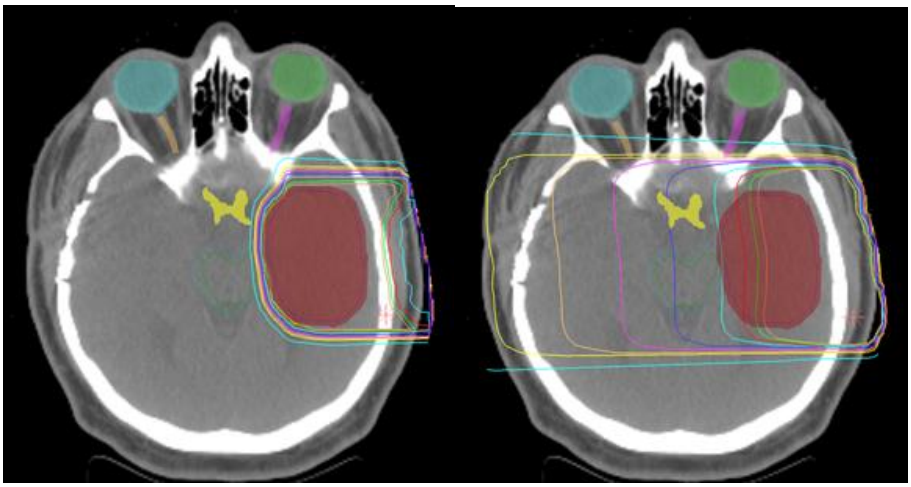

Fig. 3: Dose map from a target in the left hemisphere of the brain (shown in red) treated with a single proton beam (left) and a single x-ray beam (right). Observe the dose conformality and sharp dose fall-off of the proton plan (3).

When high-energy photons interact with matter, they do so only through indirect ionization. The photon interactions transfer energy to charged particles in the form of photoelectric, Compton, or pair production interactions. The primary interactions at diagnostic imaging energies are photoelectric and are dependent on Z^3/E^3, where Z is the atomic number of the medium and E is the incident photon energy. Photoelectric interactions have a strong dependence on Z and can be used to generate a map of relative effective atomic numbers. Protons, however, possess mass and charge, and interact primarily via direct Coulomb interactions. Proton interactions can be defined using the Bethe-Bloch equation, discussed in section 2.1 below, and are dependent on many factors, including electron density of the medium, the atomic number Z of the medium, and ionization potential of the medium. A more general way to express proton energy loss through a medium is in terms of "Relative Stopping Power" (RSP), or the amount a proton's energy is reduced while traveling through a given medium relative to the energy loss through the same thickness of water. Following the continuous slowing-down approximation (CSDA) for heavy charged particles in matter, discussed in section 2.1.2 below, protons of a given energy will deposit the bulk of that energy at the Bragg peak at an incident energy-specific depth within the target. The depth in medium where the Bragg peak occurs is closely related to the proton's "range". Proton range can

be defined at the depth where the distal falloff reaches 80% of the Bragg peak maximum, and is designated using the term R80. The R80 also corresponds to a mean of 50% of the protons coming to rest. R90, similarly defined as the range where the distal falloff reaches 90% of the Bragg peak maximum, is also used historically to define Bragg peak depth (4).[1]

The depth at which protons stop does not correlate directly to x-ray attenuation values, due to fundamentally different natures of interaction between protons and photons. CT-based x-ray imaging is commonly used to build a 3D model of the patient for treatment planning calculations. X-ray based CTs only map effective linear attenuation coefficients in the form of Hounsfield Units (HU). A conversion process from HU to RSP is required when using CT images to plan proton therapy treatments. Studies have shown this conversion process of HU to RSP to possess uncertainties between 3-4% of the proton's incident range, and in tissues such as lung and bone these uncertainties in the conversion accuracy can be even greater (5). This is cause for concern when ICRU Report 24 recommends the total uncertainty of any radiation therapy treatment be within ±5%. This makes the HU conversion process the largest source of uncertainty in proton beam treatment planning (6). RSP uncertainty is further exacerbated with CT-based artifacts such as beam hardening and streak

[1] This position is not always well-defined for protons, due to the statistical nature of particle interactions, which can cause a spread in the energy distribution known as "range straggling" (4).

artifacts caused by implanted metal. Range uncertainty is of particular importance for protons due to their finite range. Uncertainties in exact location of the end range necessitates that treatment planners to add extra margins to the distal and proximal ends of the beam range to ensure target coverage. These extra margins can add unwanted dose to healthy tissue, reducing one of proton therapy's advantages over other modalities, the sharp distal falloff. This results in planning techniques such as irradiating the entire vertebral body in pediatric CSI cases which, while still mitigating dose to the thoracic, abdominal, and pelvic regions, significantly stunts growth by inhibiting bone growth through childhood. Additionally, treatment fields for breast and lung targets risk overshooting potentially high dose through the very low-RSP lung tissue and into the heart, esophagus, and other vital thoracic normal tissue due to distally-expanded range uncertainty safety margins, as can be seen in Figure 5.

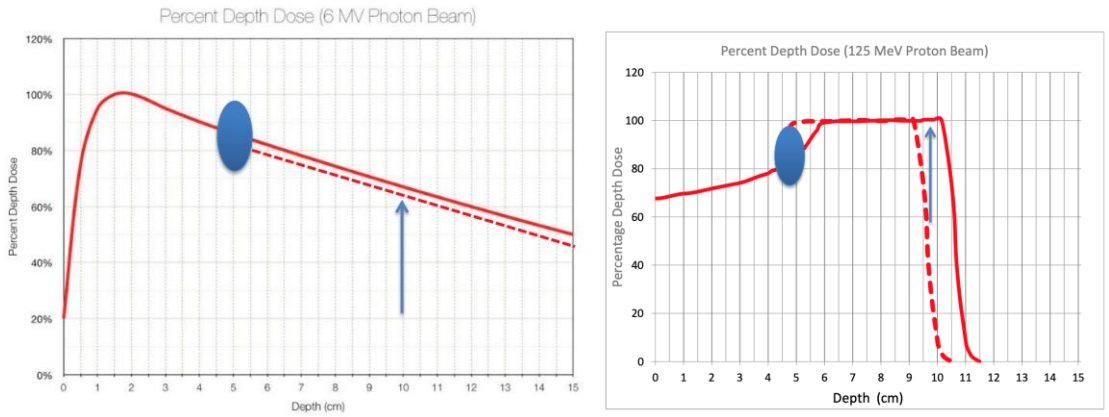

Fig. 4: A tumor at 10cm (blue arrows) treated with 6 MV photons and 125 MeV protons is obstructed by a mass proximal to it, causing a 1cm attenuation/loss of range, respectively. Due to the linear nature of photon dose deposition, the photon target only

experiences a minor loss of dose, whereas for protons the distal end of the target loses all dose.

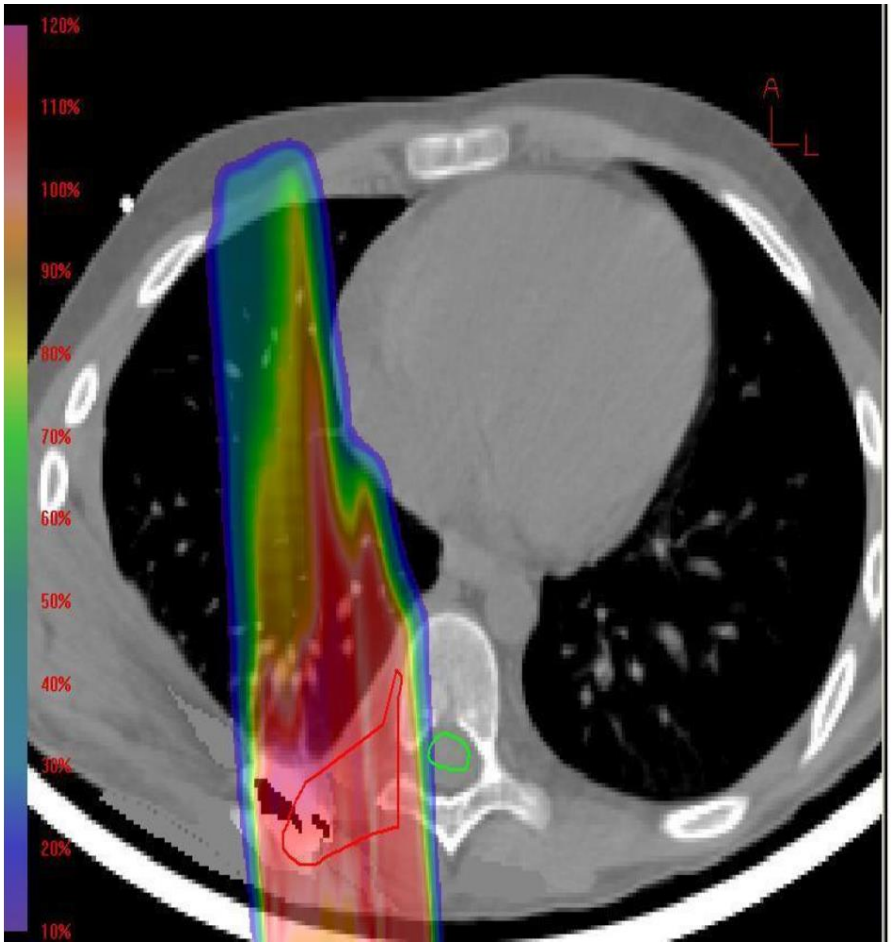

Fig. 5: An example of a proton T-spine plan over-ranging into the lung, giving unwanted dose to the right lung and heart (3).

1.2 Addressing the issue of range uncertainty

While several methods have been proposed to help better identify and reduce the uncertainty in the end range, none have proven truly comprehensive. Dual-energy CT (DECT) currently stands out as one promising solution. By using the HU from two imaging energies, one can deduce the elemental composition of materials in a scan and a more accurate map of RSP can be obtained (3). Studies by Bär et al. found that

RSP accuracy can improve to as low as 0.4% in soft tissue, as long as noise is kept low (7). However, commercially available DECT systems available today are only viable for treatment planning and diagnostic CTs, and are not practical to offer any pre-treatment patient position and range verification solutions. Furthermore, DECT is still subject to the artifacts prone to x-ray imaging. Other methods are under development, such as prompt gamma imaging, positron-emission tomography (PET) scanning of positron-emitting products of proton irradiation, to more accurately see the true range of proton beams on in-vivo targets, each of which addresses the uncertainty issue in different ways, from improving range verification to reducing uncertainty to identifying irradiated targets post-treatment. These all address the issue of range verification during or after treatment, and not beforehand or for setup.

1.3 Rationale for proton imaging

One solution that would provide an absolute ground truth of range verification in proton therapy is proton imaging. This technique was first proposed by Allan Cormack, the inventor of x-ray CT, in 1963 (8). The CT images acquired using transmission protons instead of X-rays would reconstruct as RSP "as seen by" the protons. The proton CT would produce anatomically accurate maps of stopping power and would not rely on an inherently inaccurate HU-to-RSP conversion curve. Benefits of

particle imaging would include the lack of x-ray image "artifact", as protons cannot be attenuated in high-Z, high-density material like photons. However, proton imaging may possess different artifacts. The intent of this study is to test the viability of proton imaging in comparison to X-ray imaging corrected for RSP.

The objectives of this thesis are twofold. First, to demonstrate the viability of ProtonVDA's prototype clinical proton imaging system to acquire proton radiography and proton CT systems in the clinical workflow of a proton center. Second, to compare the RSP maps generated by proton radiographs and pCT images to RSP maps calculated from traditional x-ray CT conversion methods. This thesis studies two proton imaging samples: a complex, layered sample of processed pig meat, and a fully intact pig head, along with metrics to probe quality of these image samples, discussed in chapter 3.

CHAPTER 2 - THEORY

2.1 Proton imaging general principles

Like traditional x-ray CT, proton CT presents a problem of tomographic image reconstruction in proton CT. The reconstruction process provides voxel values of RSP (defined in the previous section) instead of effective attenuation coefficients in the form of Hounsfield Units. RSP is a measure of energy lost by protons as they pass through a given region in a medium relative to the same energy loss if the medium was replaced with water. The sum of all incremental energy lost along the entirety of a single proton's path through a medium is its water-equivalent path length (WEPL). Mathematically, this can be expressed as:

$$\oint_L RSP\,(\mathrm{l})dl = \int_{E_{out}}^{E_{in}} \frac{dE}{S_w} = WEPL \tag{1}$$

where:

RSP is the relative stopping power,

L is the total path length traversed by the proton,

E_{in} and E_{out} are the energies of the proton upon entering and exiting the medium, respectively,

dE is incremental energy lost by the proton,

and S_w is the stopping power through an amount of water equal to the size of the medium.

Protons traveling through a medium lose energy via Coulomb interactions, as modeled by the Bethe-Bloch equation, discussed later in this chapter in greater detail. For practical purposes, energy lost can be related to the distance traveled by a proton via the Continuous Slowing-Down Approximation (CSDA), shown below in Figure 6.

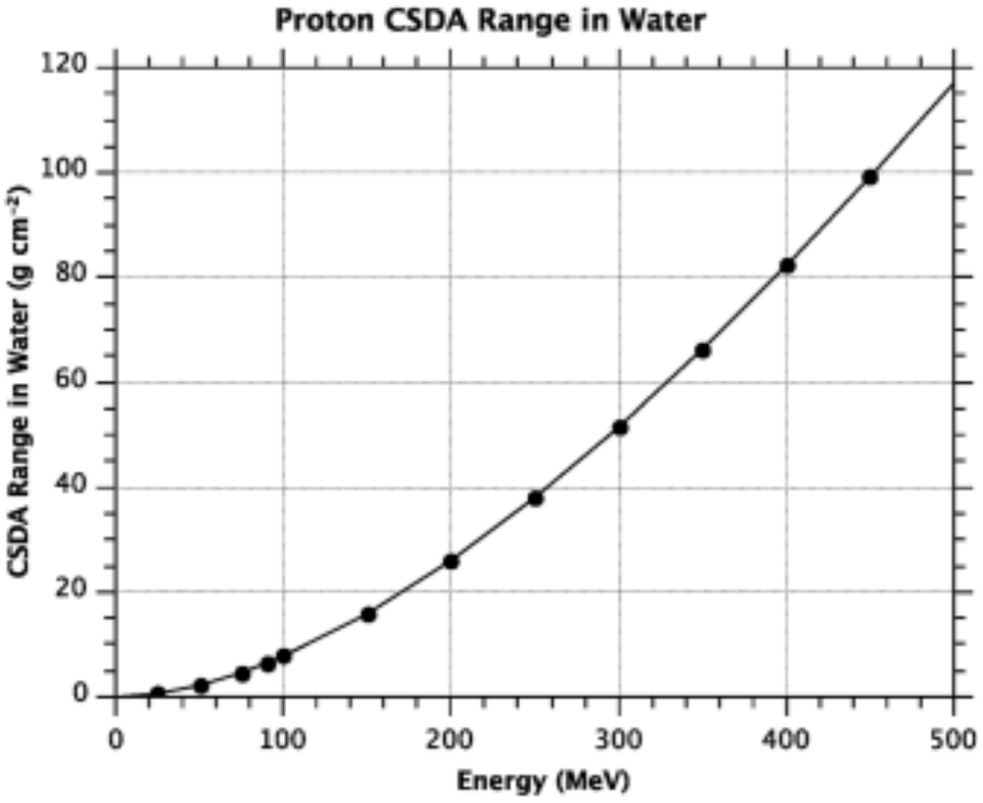

Fig. 6: CSDA range in water as a function of energy (9).

If a proton's initial energy prior to entering a medium is known along with its residual energy after traveling through that medium, the WEPL of

the proton traveled can be determined using the CSDA relationship of energy lost to distance traveled in water.

ProtonVDA's detector contains scintillating crystals capable of detecting residual energy of protons after passing through a medium. This is discussed in greater detail in chapter 3. As such, the residual energy can be subtracted from the initial energy from the proton source to acquire the energy lost within the medium. From this difference, the WEPL traveled through the target along the proton's path can be determined. This is done on an individual proton-by-proton basis for fluence on the order of 30,000-40,000 protons per square centimeter.

The WEPL provides information on the proton's scattered equivalent path length and its subsequent energy loss. WEPL does not give any information about individual voxels traversed by the proton. To convert WEPL to RSP, the voxels that each proton travels through must be known. To determine this, the physics of how protons travel through matter must be considered.

2.1.1 Multiple Coulomb Scattering

Protons lose energy traveling through an object primarily via Coulomb interactions which cause ionization and excitation of electrons within the object. Proton energy losses can be modeled by the Bethe-Bloch equation (3):

$$-\frac{dE}{dx}(\mathbf{r}) = \eta_e(\mathrm{r})\mathrm{F}(\mathrm{I}(\mathrm{r}),\mathrm{E}(\mathrm{r})) \quad (2)$$

Where:

- $\frac{dE}{\mathrm{dx}}$ is energy lost per unit distance through the target medium,

r is the vector defining the proton's movement through the medium,

η_e is the electron density of the medium relative to water, defined as:

$$\eta_e = \frac{\eta_{\mathrm{medium}}}{\eta_{\mathrm{water}}} \quad (3)$$

I(**r**) is the mean excitation potential of the medium,

E(**r**) is the proton energy, at vector position (r),

and *F* is given as:

$$\mathrm{F}(\mathrm{I}(\mathrm{r}),\mathrm{E}(\mathrm{r})) = \mathrm{K}\frac{1}{\beta^2\mathrm{E}}\left[\ln\left(\frac{2\mathrm{m_e c}^2}{\mathrm{I(r)}}\frac{\beta^2(\mathrm{E})}{1-\beta^2(\mathrm{E})}\right) - \beta^2(\mathrm{E})\right] \quad (4)$$

Where:

β is the relativistic factor *v*/*c*,

$m_e c^2$ is the electron rest mass (0.511 MeV),

and *K* is 0.17 MeV/cm.

If it is assumed that the object target will be human tissue, one can simplify $I(\mathbf{r})$ to the ionization potential of water. $I(\mathbf{r})$ has been assigned a value of 75 eV in ICRU 49. When making this assumption, equation 2 can be reduced to a simple integration:

$$\int_{E_{out}}^{E_{in}} \frac{\mathrm{dE}}{\mathrm{F}(\mathrm{I}_{water}, \mathrm{E})} = \oint_{\mathrm{L}} \eta_e(\mathrm{r})\mathrm{d}l \tag{5}$$

or, simply put, a line integral of relative electron density along the straight line of the proton track. If this were a straight-line path, this would be invertible and solvable with various analytical methods, discussed below. However, protons travel through media in randomly curving paths due to multiple Coulomb scattering (MCS). As such, the line integral shown above in Equation X is not a true "straight line path" (SLP), but a curving track with angular and positional variance. This is derived in the following subsection.

2.1.2 Most Likely Path formalism

The path protons take through media due to MCS can be considered random. As such, the approach given below is a probabilistic one that seeks to define the Most Likely Path (MLP) a given proton takes

traveling through a medium. Furthermore, the path is defined by a large number of very small random fluctuations in position and angle. This is the definition of a Gaussian distribution, and allows for straightforward manipulation of the mathematics defining MCS.

To begin, a Cartesian coördinate system for the object here defined as *t-u-v*, where *u* is the nominal beamline direction and *t, v* are the axes of the axial plane, is established. Consider a proton entering the object at depth u_0, and traversing through the object at a variable depth u_1 before exiting the distal side of the object at depth u_2, as shown below. For this explanation, it is assumed the medium is uniform water.

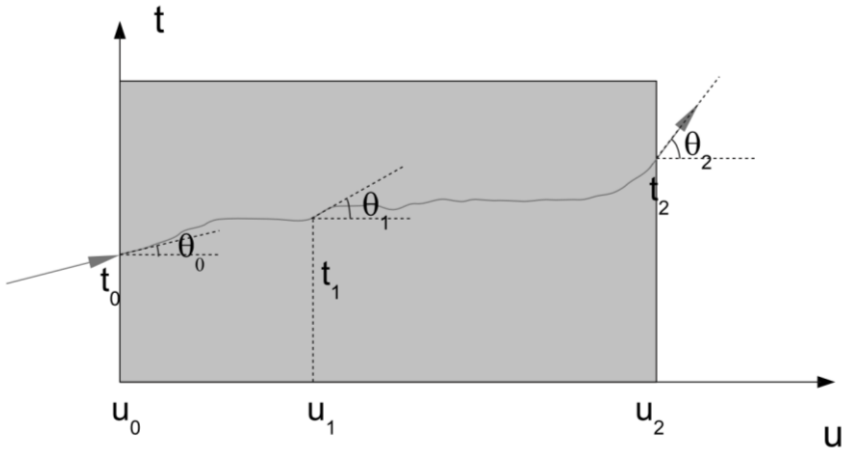

Fig. 7: Scattering geometry of an incident proton in the t-u *plane, where the* u *axis is the nominal beam direction (3).*

The position along the proton's path can be given as $t_1(u_1)$ with an angle off the central axis (CAX) given as $\theta_1(u_1)$. This lets us define a 2-D parameter for the proton's position and trajectory at depth u_1, given as:

$$y_1 = \begin{pmatrix} t_1 \\ \theta_1 \end{pmatrix} \tag{6}$$

The proximal and distal pair of detectors gives us entry and exit positions and angles. From these detectors we can obtain the parameters y_0 and y_2 for entry and exit, respectively, as shown in Fig. 6. While we would normally have to consider these parameters for both the *t-u* and *v-u* planes, these processes are wholly independent of each other, so the MLP formula derived here can simply be applied to both planes, and we can restrict the derivation to two dimensions for simplicity.

In Bayesian terms, we are seeking the maximum likelihood of y_1 given the observed information. We have three likelihoods: 1.) a "prior" likelihood of finding the proton at y_1 knowing its entry position y_0 (in other words: what the path "should" be given the entry information), 2.) a likelihood of finding the proton at the exit y_2 given y_1, and 3.) a "posterior" likelihood of finding the proton at any point in the medium given the exit parameter y_2 (in other words: a constraint on the prior likelihood given by the exit parameters). Rewriting this in the form of Bayes's Theorem,

$$\mathrm{L}(\mathrm{y}_1|\mathrm{y}_2) = \mathrm{L}(\mathrm{y}_2|\mathrm{y}_1)\mathrm{L}(\mathrm{y}_1|\mathrm{y}_0) \tag{7}$$

In the above notation, *L(x | y)* would refer to the likelihood of the parameter x given the known likelihood of parameter *y*. To maintain terminology, we are seeking the most likely parameters of y_1 given the entry y_0 and exit parameters y_2. Mathematically, this is represented as:

$$L\left(y_1 = y_{MLP} \middle| y_2 \right) = max \tag{8}$$

$$or$$

$$\nabla L\left(y_1 = y_{MLP} \middle| y_2 \right) = \begin{pmatrix} \partial t_1 \\ \partial \theta_1 \end{pmatrix} L\left(y_1 = y_{MLP} \middle| y_2 \right) = 0$$

As mentioned in the previous section, the Fermi-Eyges Gaussian approximation for MCS likelihood of a given proton will be used here. In its general form, it is written as:

$$L\left(y_1 \middle| y_0 \right) = exp\left(-\frac{1}{2} y_1^T \Sigma_1^{-1} y_1 \right) \tag{9}$$

Where:

y_0 is the null starting parameter,

T is the matrix transpose,

and Σ is a scattering matrix that describes the variances and covariances of the parameters of *y*,

$$\Sigma_1 = \begin{bmatrix} \sigma^2_{t_1} & \sigma^2_{t_1\theta_1} \\ \sigma^2_{t_1\theta_1} & \sigma^2_{\theta_1} \end{bmatrix} \tag{10}$$

As mentioned at the beginning of this section, the angular dispersion of a proton at any given point in a medium due to Coulomb interactions is effectively random and is generally small in magnitude. As such, it can be considered a normal distribution. The generalized standard deviation of such a distribution is given by the Fermi-Eyges equation (10) and augmented by Lynch and Dahl in 1991 with the appropriate constants:

$$\sigma(\mathrm{l}, E) = \frac{13.6}{\beta(\mathrm{E})\mathrm{p}(\mathrm{E})}\sqrt{\frac{\mathrm{l}}{\mathrm{X}_0}}\left[1 + 0.038\mathrm{l}n\left(\frac{\mathrm{l}}{\mathrm{X}_0}\right)\right] \tag{10}$$

Where:

u_0 is the entry depth (generally zero),

u_1 is the depth in question,

β is the relativistic ratio v/c,

p is the proton momentum,

13.6 MeV and 0.038 are the empirical constants found by Lynch and Dahl (11),

and X_0 is the "radiation length": an intrinsic quantity of a medium equal to the distance a charged particle must travel to lose all but $1/e$ of its energy. For our purposes, we use the radiation length of water, 36.1 cm. From this, the positional and angular variances can be established:

$$\sigma_{t_2}^2(u_1, u_2) = \frac{13.6}{X_0}\left[1 + 0.038ln\left(\frac{u_2 - u_1}{X_0}\right)\right]^2 \int_{u_1}^{u_2} \frac{(u_2 - u)^2}{\beta(u)p(u)}\,du \quad (11)$$

$$\sigma_{\theta_2}^2(u_2, u_1) = \frac{13.6}{X_0}\left[1 + 0.038ln\left(\frac{u_2 - u_1}{X_0}\right)\right]^2 \int_{u_1}^{u_2} \frac{1}{\beta(u)p(u)}\,du \quad (12)$$

$$\sigma_{t_2\theta_2}^2(u_2, u_1) = \frac{13.6}{X_0}\left[1 + 0.038ln\left(\frac{u_2 - u_1}{X_0}\right)\right]^2 \int_{u_1}^{u_2} \frac{u_2 - u}{\beta(u)p(u)}\,du \quad (13)$$

Per Bayes's Theorem presented at the beginning of the section, we can now define the likelihood of y_1 given the exit constraint y_2 by combining the above two likelihoods:

$$\mathrm{L}(y_1|y_2) = \exp(-\frac{1}{2}\Big((y_1^T - y_0^T R_0^T)\Sigma_1^{-1}(y_1 - y_0 R_0) + (y_2^T - y_1^T R_1^T)\Sigma_2^{-1}(y_2 - y_1 R_1)\Big)) \quad (14)$$

This can be rewritten using the definition of chi-squared as the averaged sum of squared errors:

$$L(y_1|y_2) = \exp(-\chi^2) \quad (15)$$

We thus seek to minimize chi-squared in order to acquire maximum correlation between y_1 and the most likely path. We set the differential of chi-squared with respect to t_1 and $\square_1$ equal to zero to find the minimum chi-squared value,

$$\chi^2 = \frac{1}{2}((y_1^T - y_0^T R_0^T)\Sigma_1^{-1}(y_1 - y_0 R_0) + (y_2^T - y_1^T R_1^T)\Sigma_2^{-1}(y_2 - y_1 R_1))$$

$$\chi^2 = \frac{1}{2}(y_1^T y_1 \Sigma_1^{-1} - 2y_0^T R_0^T \Sigma_1^{-1} - y_0^T R_0^T \Sigma_1^{-1} y_0 R_0 + y_2^T y_2 \Sigma_2^{-1} - 2y_1^T R_1^T \Sigma_2^{-1} - y_1^T R_1^T \Sigma_2^{-1} y_1 R_1)$$

$$\nabla\chi^2 = (\Sigma_1^{-1} - R_1^T\Sigma_2^{-1}R_1)y_1 - \Sigma_1^{-1}R_0y_0 - R_1^T\Sigma_2^{-1}y_2 = 0$$

Then solve for y_1 to find the most likely path,

$$y_{1=MLP} = (\Sigma_1^{-1} - R_1^T\Sigma_2^{-1}R_1)^{-1}(\Sigma_1^{-1}R_0y_0 - R_1^T\Sigma_2^{-1}y_2) \quad (16)$$

which is used in both ProtonVDA's iterative solver as well as their GEANT4 simulation toolkit.

2.2 Imaging theory general physics

The intent of proton CT is to determine RSP per voxel. If we consider the target a 3-D collection of voxels, each with their own RSP, the problem to solve becomes a complex multi-variable one, with a number of solutions equal to the number of voxels in the target (~10^6), and a number of equations equal to the number of protons (~10^9). However, these "equations" are very sparse, as most protons will only travel through ~$10^{2\sim3}$ voxels on their path.

To put this in mathematical terms, the RSP values of every voxel can be linearized in a M-dimensional matrix **x**, and the total WEPL traversed by each proton can be linearized into a N-dimensional matrix **b**. A "system

matrix" **A** with dimensions M x N can be constructed, each cell corresponding to the path length traveled by each proton through each voxel. As such, the problem of solving for the RSP value of each voxel can be written simply as:

$$Ax = B \tag{17}$$

with the goal of solving for the one-dimensional matrix **x**. As mentioned above, however, each proton will only travel through ~$10^{2\sim3}$ voxels along their path, so the matrix **A** will be incredibly sparse. The most commonly utilized methods to solve the system matrix for the corresponding problem in tomographic x-ray image reconstruction are filtered backprojection and iterative reconstruction. Filtered backprojection transforms the sinogram of the object into Fourier frequency-domain space, applying filters as desired to adjust and augment low-frequency "coarse" detail and high-frequency "fine" detail, then reconstructing the 2-D image via the inverse Fourier transform. While viable for our purposes, this method would require the proton paths to be straight lines, which is acceptable as an approximation but we know is not true, due to MCS. A Fourier transformation on the line integral thus assumed to be the proton path would be inherently inaccurate on two

levels: the approximated path is not a straight line, and the end point of the proton would not be accurate. Additionally, from a mathematical perspective, filtered backprojection is less effective on sparse datasets (12), and the system matrix would be incredibly sparse - each individual proton only touches $10^{2\sim3}$ out of the 10^6 voxels. Iterative reconstruction, on the other hand, turns the problem into a simple algebraic one that works better with more variables and sparser matrices. This method is vastly preferred for the purpose of proton image reconstruction and will be explained below, in particular demonstrating three methods used by ProtonVDA's image reconstruction algorithms: diagonally-relaxed orthogonal projections (DROP) (13) and component-averaged row projections (CARP) (14), each based on the fundamentals of Algebraic Reconstruction Techniques (ART).

2.3 Iterative reconstruction techniques

The problem of iterative reconstruction is one of linear algebra. Namely, one seeks to solve for individual values of a matrix if one knows the sums of their rows and columns. A very simple exercise demonstrating the concept is shown below (15). Take a weighted average of the sums of the rows, assigning them to the individual values of the system matrix, then adjusting along the rows or columns based on the new sums as deemed appropriate.

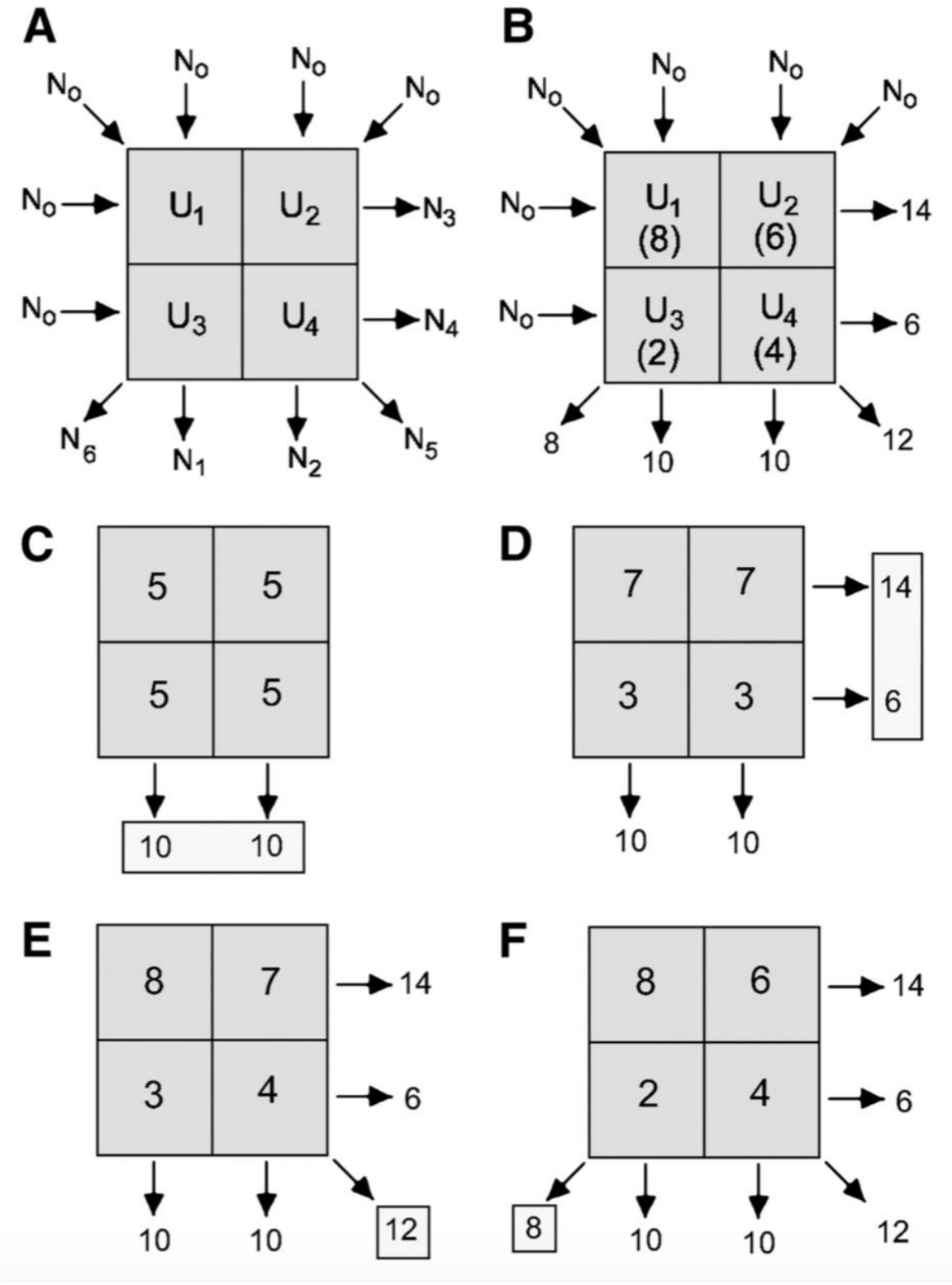

Fig. 8: A simple ART iterative algorithm for a 2x2 matrix (15).

In the case of our system matrix, the rows correspond to the individual voxels of the 3-D target, and the columns correspond to the RSP traveled through for each individual proton. The RSP values, linearized, make up our **b** matrix above. We also know from the upstream and downstream detectors, in conjunction with the MLP calculation, the paths the protons took through the target, and which voxels they intersected. As mentioned above, these 1mm^3 voxels will be assumed to each have constant RSP values. The system matrix cells will begin with a value equal to the distance traveled within each voxel by each proton, and 0 otherwise. This leaves us with the unknown **x**, the linearized array of RSP values for each voxel. Three methods below for solving this iterative problem are explained, each in use by ProtonVDA's calculation software.

2.3.1 ART

A method originally proposed by Kaczmarz (16) and developed by Gordon, et al. (17), Algebraic Reconstruction Techniques (ART) looks to solve a matrix system via repeatedly updating closer and closer estimates at the "ideal" solution. Starting with an estimate for $\mathbf{x_0}$ at a given row *i*, it takes the inner product of $\mathbf{x_0}$ with the *i*th row of **A**, $\mathbf{A_i}$, which should result in the *i*th value of **b**, $\mathbf{b_i}$. Inevitably this will be off by a certain amount, unless your guess is particularly lucky. It then "updates" $\mathbf{x_0}$ by adding the difference of b_i and $\langle \mathbf{A_i}, \mathbf{x_0} \rangle$, averaged over $\mathbf{A_i}$ with a "relaxation factor" λ

to control the rate of convergence, to result in a new "guess" for $\mathbf{x_0}$, $\mathbf{x_1}$. This process iterates through every row $\mathbf{A_i}$, then iterates across the whole matrix a user-defined number of times. Mathematically, this can be expressed as:

$$x_{n+1} = x_n + \lambda \frac{b_i - (A_i \cdot x_n)}{|A_i|^2} \tag{18}$$

Where *n* is the iteration of **x**, separate from *i* due to the possibility of iterating through the entire matrix multiple times. Naturally, for a system matrix with on the order of 10^9 rows, this is an immense amount of data to process, and not feasible for anything other than a supercomputer to process in a meaningful timeframe for clinical use (on the order of seconds). Luckily, two other methods are employed to modify the ART technique in a way that eases computational load, discussed below.

2.3.2 DROP

Diagonally-relaxed orthogonal projections (DROP) is an iterative solving technique for sparse matrices proposed by Aharoni and Censor in 1989. While fundamentally rooted in the ART technique, DROP breaks the system matrix **A** into *m* "blocks", designated as $\mathbf{A} = I_1 \cup I_2 \cup I_3 \cup \ldots \cup I_m$

which are then solved through per the ART algorithm above instead of iterating through individual rows. The value of *m* is determined by the user, where a higher value is indicative of more solving steps but higher image resolution, converging closer to the ART results as *m*→M total voxels. DROP also includes a unique relaxation factor U_m, a diagonal matrix that weights each row's adjustment by an amount inversely proportional to the amount of non-zero values in that block. Mathematically, the DROP method can be expressed as:

$$x_{n+1} = x_n + \lambda U_m \left[\sum_{i \in I_m} \frac{b_i - (A_i \cdot x_n)}{|A_i|^2} A_i \right] \tag{19}$$

with U_m given as:

$$U_m = diag[\min(1, s_m^{-1})] \tag{20}$$

where s_m is the number of non-zero elements in I_m. While simplifying the problem of iterative reconstruction, the process still functions serially - namely, x_n must be updated with each iteration before the next block can be processed.

2.3.3 CARP

Developed by Gordon and Gordon in 2005, Component-Averaged Row Projections (CARP) is a variant on ART designed for parallel processing. It begins from the fundamental concept of ART, but instead of updating $\mathbf{x_n}$ for each row of the system matrix **A**, the same $\mathbf{x_n}$ is applied to each row separately, then the updates to $\mathbf{x_n}$ are added together, as a weighted average based on how many non-zero entries were in each respective row. Mathematically, this can be represented as:

$$y_m = x_n + \lambda \frac{b_i - (A_i \cdot x_n)}{|A_i|^2} A_i \tag{21}$$

where $\mathbf{y_m}$ is the partially-updated $\mathbf{x_n}$ for a given block *m*. Each $\mathbf{x_n}$ can then be given as:

$$x_{n+1} = s_m^{-1} \sum_m y_m \tag{22}$$

with s_m as defined above.

In a comparison of DROP and CARP reconstruction of GEANT4 simulated images performed by Saroj Rai at Northern Illinois University in 2015, he demonstrated that both algorithms produce viable images. He noted, however, that DROP images were somewhat "smoothed" - not enough to be clinically relevant but enough to be noticeable, while CARP images were crisper and had higher contrast on edges, at the cost of higher noise (18). Total variation superiorization (TVS) analysis on each image set, along with relative error calculation and voxel-level statistical analysis, showed very similar quantitative results between the two. ProtonVDA currently uses all three calculation methods for their image studies.

2.4 The Limited-Angle problem

A notable issue protons suffer from an imaging standpoint is their limited depth of penetration. As discussed prior, a clinical proton imager would utilize the proton accelerator of the clinic instead of supplying a separate source of protons. Most clinical cyclotrons and synchrotrons today operate between 200-250 MeV, corresponding to a maximum penetration depth of 35cm (19). While this is suitable for head and neck, thoracic, extremity, and pediatric imaging, adult pelvic regions, as well as thoracic areas in large adult patients, can exceed this thickness. While a maximum range of 35cm is clinically acceptable for proton treatment,

proton imaging requires that the Bragg peak be deposited outside the patient in a range detector. Furthermore, a minimum amount of residual range will be required in order for the range detector to register a deposited Bragg peak. Wang, et al. suggest 50 MeV residual for high-quality range verification, corresponding to an equivalent range of 2.23 cm. From this, the actual CSDA range a 200 MeV proton will be allowed to travel through a patient is 23.73 cm, limiting the maximum depth further. An example is shown in Figure 8, turning the problem of limited range into a problem of limited angle reconstruction.

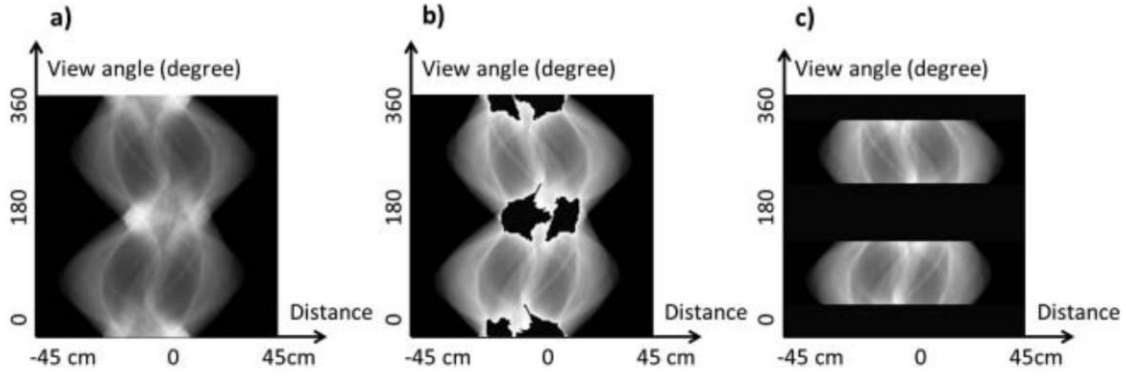

Fig. 9: A proton radiograph sinogram of a pelvic phantom. A: computer reconstruction of proton sinogram, B: the same sinogram with regions missing corresponding to the range cutoff of 200 MeV, C: the same sinogram with the angular tracks of the missing regions removed entirely (20).

The problem of limited angle image reconstruction is not a novel one in the field of tomography, however the setting of proton imaging offers some unique solutions. Much work has already been done with iterative tomographic image reconstruction using limited views (21). One proposed solutions is using pRad in conjunction with a kV scan to "correct"

the HU-RSP conversion (22). Filling in the missing fields of view with MV scans has also been suggested. Scattering interactions are predominant in both proton interactions and high-energy x-ray interactions, and thus yield closer physical results (20). While these may provide alternative promising routes to solve the problem of maximum range limitation, they will not be the focus of discussion in this paper.

CHAPTER 3 - MATERIALS AND METHODS

3.1 General equipment setup

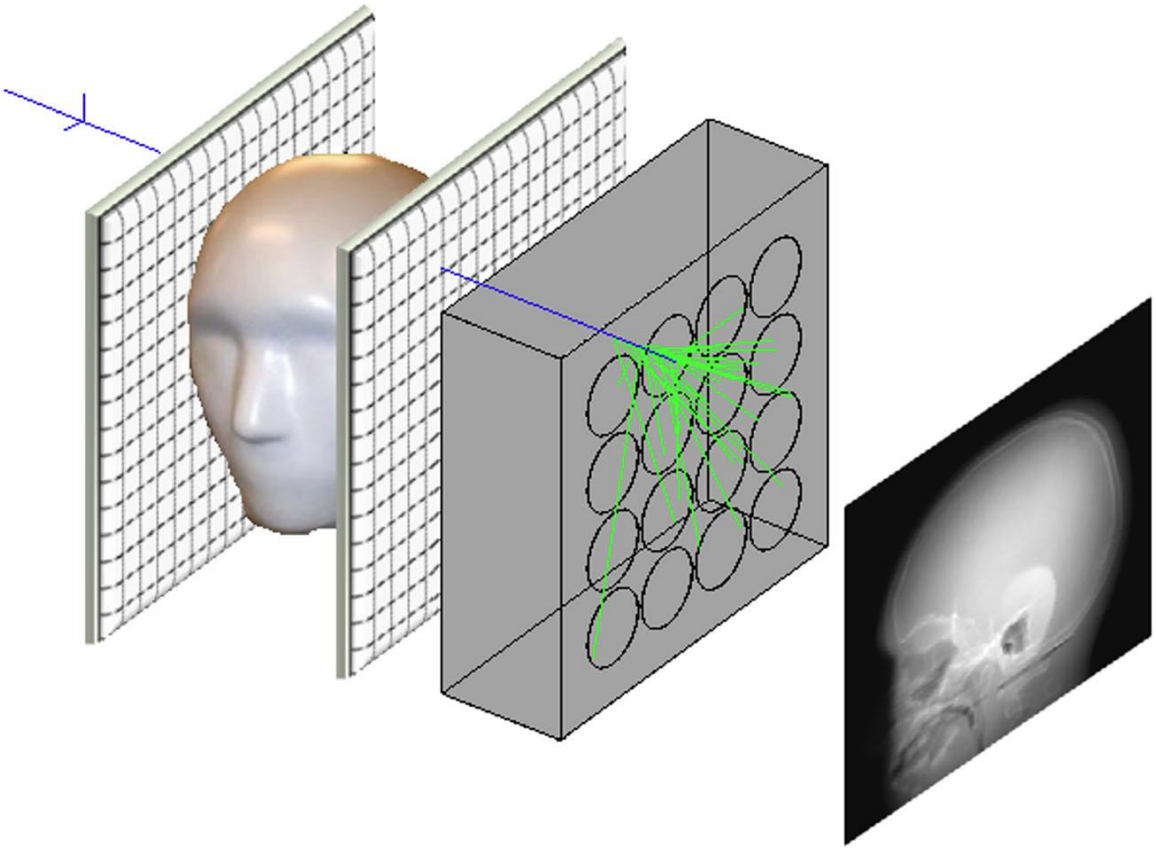

Fig. 10: A conceptual schematic of the proton detector, showing path tracking both proximal and distal to the patient with residual range measurements upstream, resulting in the sample radiograph shown on the right for a pediatric head phantom (12).

The Phase II pCT scanner in use by ProtonVDA was built in conjunction with Northern Illinois University (NIU) and Fermi National Accelerator Laboratory (FNAL). The phase II scanner was modeled after the Phase I scanner built in conjunction with Loma Linda University, NIU,

and University of California Santa Cruz (3, 12, 18, 22). A very generalized conceptual schematic of the detector is shown above in Figure 10. Two tracking detectors are placed proximal (upstream) and distal (downstream) to the target. The trackers utilize silicon-strip detector (SSD) technology. While more costly than plastic scintillators, SSDs offer near 100% efficiency for charged particle detection. They feature minimal noise, fine spatial resolution, simple and robust calibration, and are easy to mill without utilizing hazardous or toxic chemicals (23). The two proximal trackers are 20 x 24cm in size, the distal trackers 24 x 30cm, held together tightly in a solid aluminum frame. Production tests measured between 99.2% and 99.5% efficiency on the detector planes. This factors in 0.6mm gaps between the milled SSD strips which account for ~0.4% of the efficiency loss. The radiological thickness of the SSDs is well modeled and factored into the residual range calculation. Production tests of the strip material as originally used in Fermilab's Fermi-LAT SSD found 0.066mm root-mean-square spatial resolution per coördinate measured (23). Additionally, measured noise is 40 times below the signal expected for 200 MeV protons. The silicon strip detectors are read out by a custom-printed circuit board connected to fifteen field programmable gate array (FPGA) chips. The last of which, an Xilinx™ Vertex-6 chip, acts as the event builder and connects directly to the data acquisition computer via a 100Mbps ethernet cable. Tests for dead time of signal tracking at an event rate of

1.3MHz resulted in a trigger rate of 1.6MHz, with a dead time fraction of 25%. Lowering the event rate to 1MHz (1 million protons per second) resulted in a dead time fraction of under 10% (12).

The range detector is placed immediately downstream of the distal SSD positional detectors, and is used to measure the residual energy of the imminent protons. The range detector consists of five layers of UPS-923A polystyrene-based scintillator material at 10 x 40 x 5.1cm thickness for each layer. Each is read out by a R3318 Hamamatsu photomultiplier tube. These are connected to two custom-printed circuit boards, one reading three of the five channels and one reading two. Signal triggers from imminent protons can be read across all five layers, but are primarily read across the first layer, as every proton will enter that layer at a minimum.

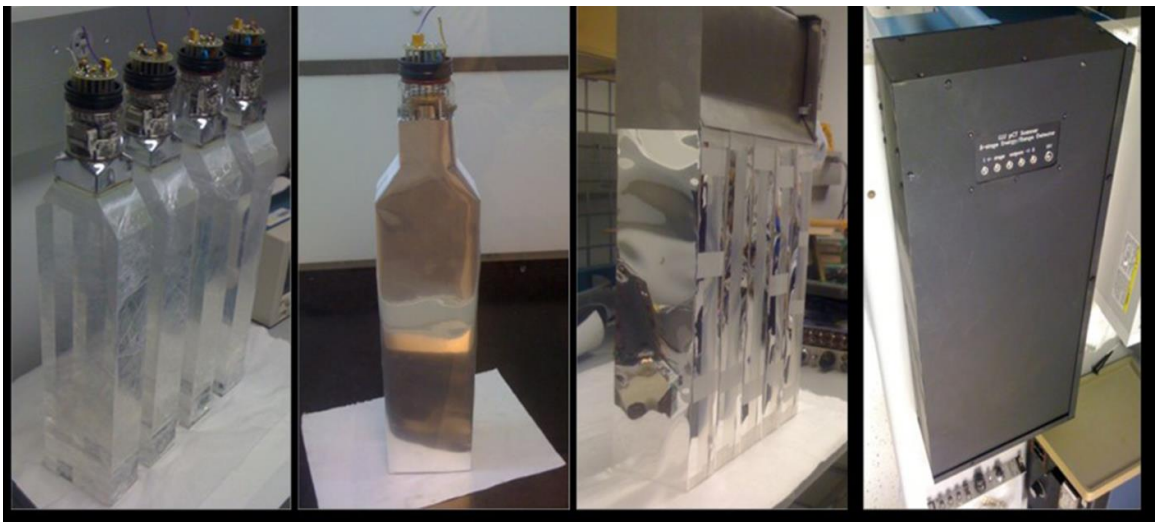

Fig. 11: From left to right: Four scintillator layers with PMT visible, a singular scintillator layer, all five layers together, and the processor. (23)

The imaging system as a whole is referred to as "monolithic" due to its nature as a complete, coherent unit, as compared to a modular or segmented unit with separate parts.

3.1.1 SSD position calibration

Initial calibration of the pCT scanner takes place in two parts: a quick calibration of the SSD trackers, and a more complex calibration of the range detectors. The concept of the SSD tracker calibration is simple: the accelerator operator creates a plan of some amount of pencil beam "spots", or beamlets, in a known configuration. These spots have relatively low fluence for quick delivery. The proton intensity is not as important so long as the trackers are able to positively detect the location of the spots. For the purposes of these image tests, the calibration field had 25 PBS spots fired at 230 MeV delivered in under a second. The measured spots on the four upstream and downstream detector planes are compared to the known spots from the accelerator plan. A Levenberg-Marquardt non-linear optimization is performed to transform the coördinate system of the measured spots to the known accelerator plan spots, via an in-house program called "Weplator" (22). The transformation effectively converts one *n*-dimensional coördinate system into another using iterative multi-

variable techniques and once a solution is reached provides a stable algorithm to translate points of one system into another (24).

3.1.2 Range detector calibration

Besides positional calibration, a series of measurements to calibrate the WEPL are performed on the pCT before each imaging session. A set of triangular "step phantoms" are set up lengthwise as shown below (25). These consist of three pyramids of 6.35mm steps in the beam direction a total of eight times for a full height of 50.8mm. Four polystyrene slabs of 50.8mm thickness are set in sequentially to measure the full range of 200MeV protons and ensure that each of the five stages of the range detector are calibrated in turn. A quadratic parametrization of PMT response based on event position within the scintillator has been calculated with GEANT4 (GEometry ANd Tracking 4). The parametrization is applied in conjunction with the MLP calculation for proton deposition position to PMT readout in order to remove positional dependence from PMT readings. The spatial variance in PMT readout with this correction has been shown experimentally to be under 0.5% RMS (23).

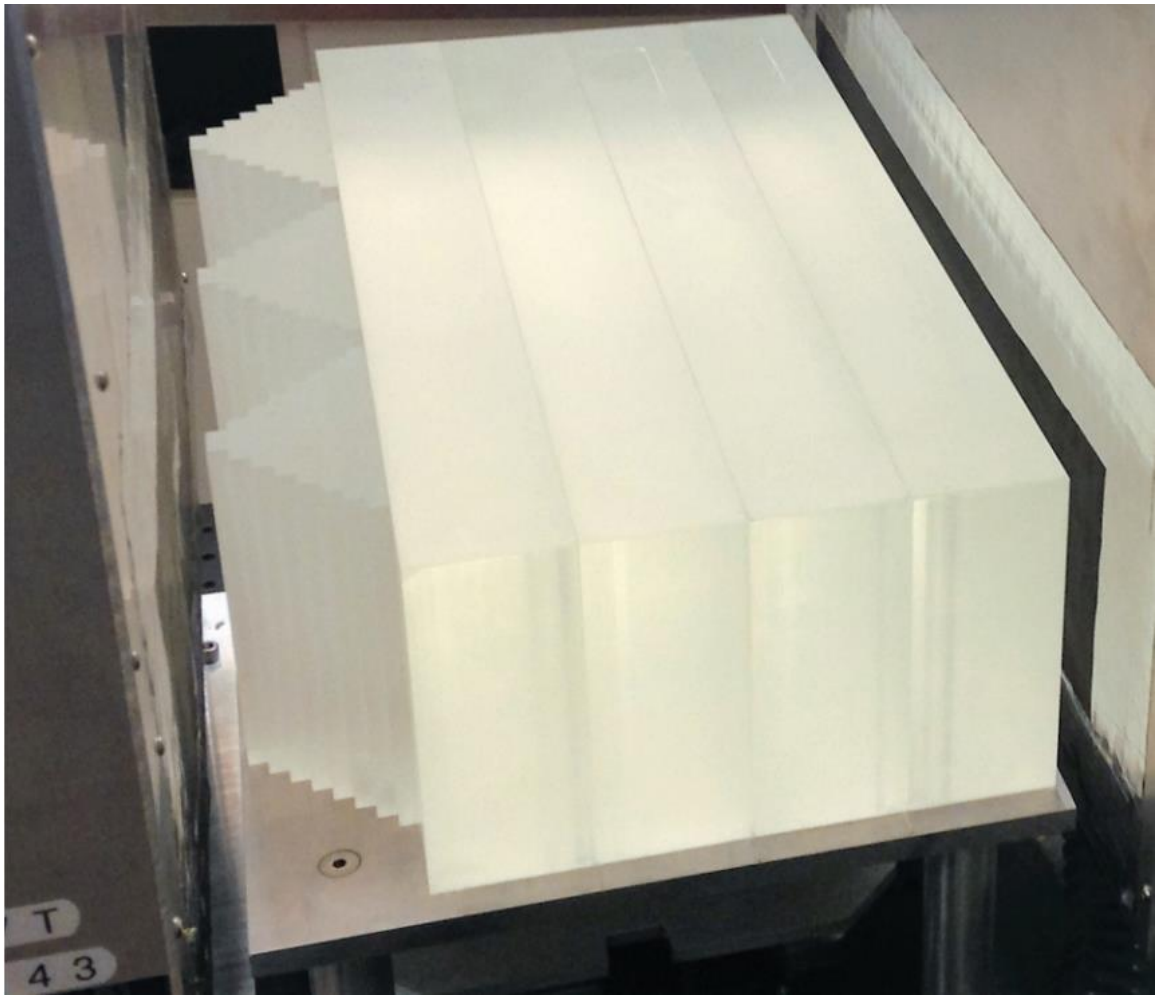

Fig. 12: The WEPL step calibration phantom, showing both the pyramid steps and the four 50.8mm polystyrene bricks (23).

The actual calibration is a three-part process on a proton-by-proton basis. First, the path of each proton is calculated using the SSD tracker readouts and MLP calculation. The WEPL traveled by the proton is then determined by multiplying the RSP values of air and polystyrene by the total distance traveled through each along the path. This is matched up to the PMT range detector readout, corrected for positional dependence via the quadratic parametrization mentioned above. These readouts are then fitted with a Gaussian to find the mean value and variance of the

response. Figure 13 below shows a WEPL-energy graph with second-order polynomial fit curves (25).

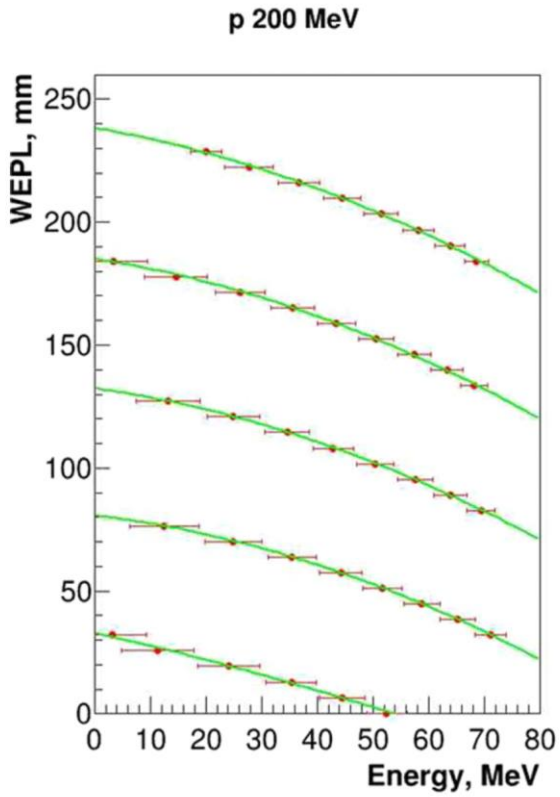

Fig. 13: Experimental calibration curves for the five-stage range detector (25).

3.2 Clinical requirements

The most important aspect of clinical viability is that the imaging system be able to interface with the native proton beamline. Cyclotrons and synchrotrons are the only devices currently clinically available to produce protons at high enough energy and intensity for patient treatment. With present technology, these devices are far too large to adapt to a stand-alone imager. As such, the imaging system must be able

to work with whatever modality and energies are present in the beamline. Historically, passive and broad beam scattering have been used for proton treatment, utilizing spread beams via passive scatter or active scanning, sometimes called "uniform scanning". These spread beams are then collimated in two dimensions using a brass or CerroBend aperture, and shaped in the distal dimension with a wax compensator. However, over the past decade the standard of care for modern proton centers has shifted to pencil-beam scanning (PBS). This uses high precision steering magnets to rapidly "paint" the target area with beamlets, or "spots", several millimeters in diameter. This precise aiming can eliminate the necessity for the aperture and compensator to shape the beam, though apertures can still be used to sharpen spot penumbras. A clinically viable proton imager to be sold on a mass scale must be compatible with PBS delivery at the energies the site can provide, which are often higher than passive scattering or active scanning modality sites. While much more complex from an engineering standpoint and more prone to discrete clinical errors, this modality does allow for the unique and very simple positional calibration of the trackers, discussed in the previous subsection.

From an imaging standpoint, the images must be both high quality and highly accurate. "Quality" here refers to the sharpness of the image and ability to discern anatomical landmarks used for planning and patient setup. This can be discerned visually via direct visual comparison

of regions of interest. This parameter can be difficult to quantify. Welsh et al.'s and Miller et al.'s studies comparing reconstructed proton RSP images of human targets demonstrated that clinical oncologists deem the visual quality adequate for planning and patient setup (26, 27). In this paper, the scans will be compared in regions of interest to directly assess this visual quality. "Accuracy" refers to RSP accuracy, which Schulte et al. suggest be within 1% (3).

The signal-to-noise ratio must be high enough for the detector to generate quality images without overdosing the patient, as well as sufficient contrast and sharpness to enable therapists to align appropriate anatomical targets while keeping dose to the patient suitably low. Testing with the protonVDA system suggests dose to the patient from proton imaging would be ~1% of the dose of corresponding x-ray imaging methods, on the order of 1.5 mSv for pCT and 10 μSv for pRad (26). Besides quality, the image acquisition and creation must fall within a clinically relevant timeframe: Schulte, in his 2018 proof of concept presentation, suggests <1 minute for pRad acquisition for alignment and <10 minutes for pCT acquisition for treatment planning, as low as 3 minutes for live adaptive planning. To match the industry standard x-ray CT and radiograph timeframes, a timeline of seconds for pRad and under 2 minutes for pCT is more clinically reasonable, if less feasible.

3.3 Experimental setup

The scans took place at the Northwestern Medicine Chicago Proton Center, located in Warrenville, Illinois. The center utilizes an IBA cyclotron and four treatment rooms. The measurements took place in its fixed-beam room, utilizing a pencil-beam nozzle and a gantry fixed at 90 degrees relative to vertical. The room's treatment table is mounted on a robot arm built by Forte Robotics (now owned by Ion Beam Applications (IBA)), with six degrees of freedom and millimeter-level positional resolution confirmed via monthly and annual QA, along with regular preventative maintenance (PMs) performed by the on-site IBA operators. For both measurements, the tracking panels and range detector were mounted on this robot then aligned to isocenter via in-room lasers, as shown below.

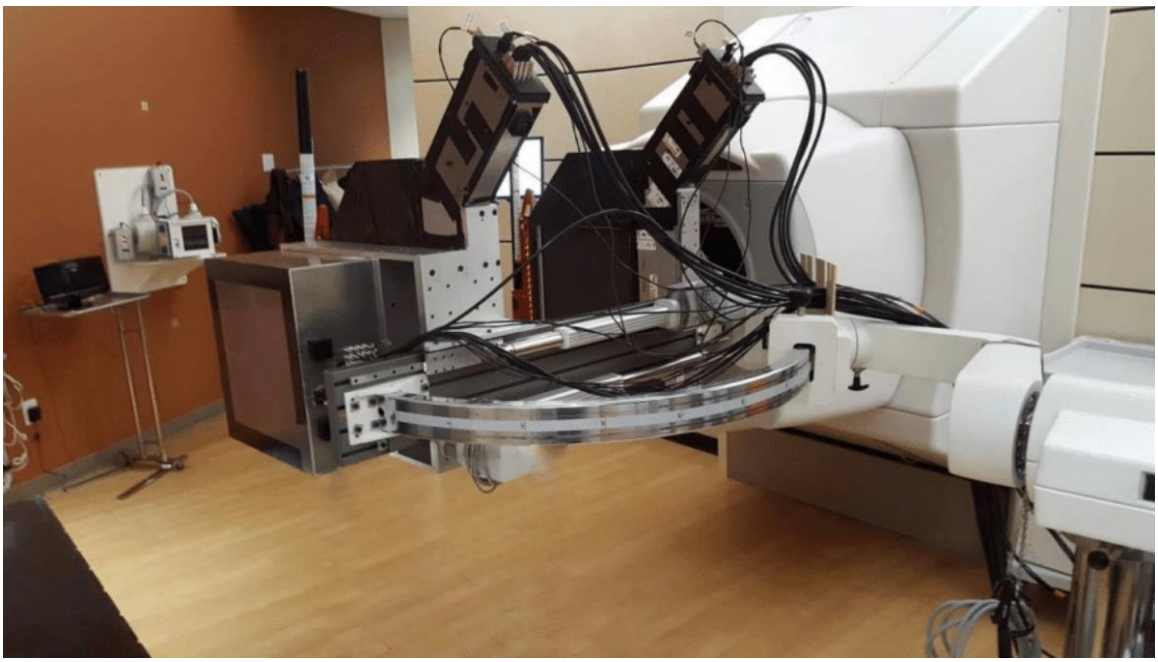

Fig. 14: In-room setup at Northwestern Medicine Proton Center (NMPC) Room 1 (3).

The pig shoulder and rib tissue samples were vacuum sealed and stored in a wax bucket of known radiological thickness, shown in Figure 15 below. Alignment via in-room lasers and radio-opaque bebes set for consistent alignment between the x-ray CT and proton CT setups was performed.

Fig. 15: Setup of pork tissue samples.

The pig head was vacuum-sealed and cast in an Alpha Cradle® mold foaming agent by VanArsdale (shown in figures 16 and 17), commonly used for patient immobilization. This allowed for easy and reproducible placement between the multiple physical scanning locations. Tape with radio-opaque bebes was applied to the upper surface and aligned based on lasers from the first x-ray CT performed. These were then used to align for the proton CT to ensure consistent setup. The raw proton images for both tissue samples were acquired as a series of ninety radiographs taken at four degree intervals on a calibrated rotating stand between the two pairs of detectors, as seen in figure 18. These were then reconstructed into a tomographic 3D image via the GEANT4 code used by ProtonVDA and converted into DICOM format via Dicompyler, a custom software written by Aditya Panchal of Amita Health.

Figs. 16 & 17: Pig head setup in Alpha Cradle® immobilization device with laser alignment by bebes.

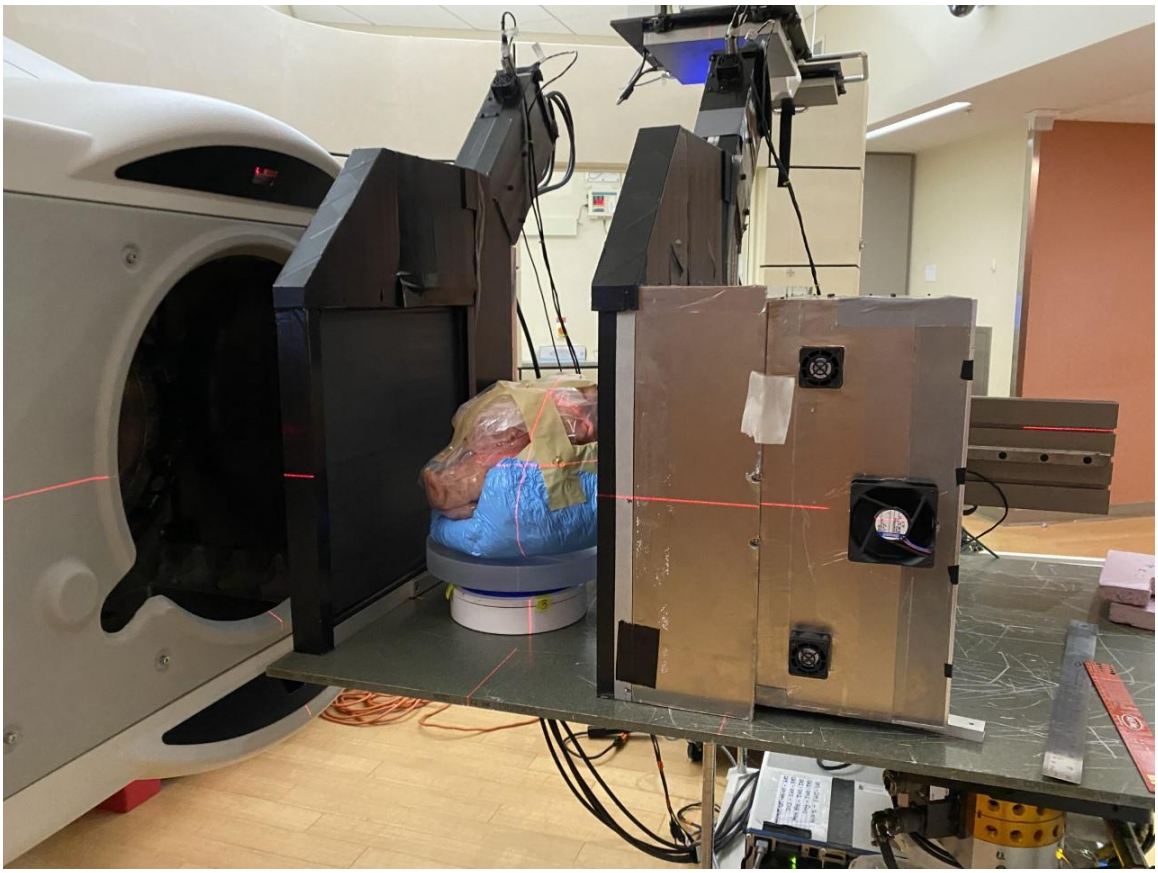

Fig. 18: Pig head pCT setup on rotating stand in NMPC Room 1.

3.4 Analysis and recapitulation

The aims of this thesis are twofold, as addressed in chapter 1: to demonstrate the viability of pCT in the clinical setting, and to compare x-ray CT images of tissue samples with pCT images, with the specific intent of addressing proton range uncertainty brought about by x-ray scans. To this end, relevant parameters must be considered regarding physical accuracy of the image as well as usefulness in visually defining targets. The x-ray CT images of both samples were resampled from HU to RSP via a

conversion curve for clinical use acquired by stochastic calibration at the time of CT commissioning. As mentioned in the previous section, Schulte suggests WEPL and RSP resolution better than 1% for clinical functionality. This was tested for via voxel comparisons within regions of interests (ROI) in bone, muscle, fat, and air tissues. Differences in RSP were created via image subtraction between selected slices with the Velocity image analysis program as well as single-spot plans over both volumes created with the RayStation™ treatment planning program, version 9A. Line dose profiles along the central axis of each spot were taken in areas of soft tissue, high-Z material, and irregular density areas such as the sinuses of the pig head, in order to directly compare range uncertainty. Non-uniform areas, particularly where tissue borders air-filled cavities, are of particular interest as these are regions where the risk of over-ranging is highest.

CHAPTER 4 - RESULTS

4.1 Calibration and initial results

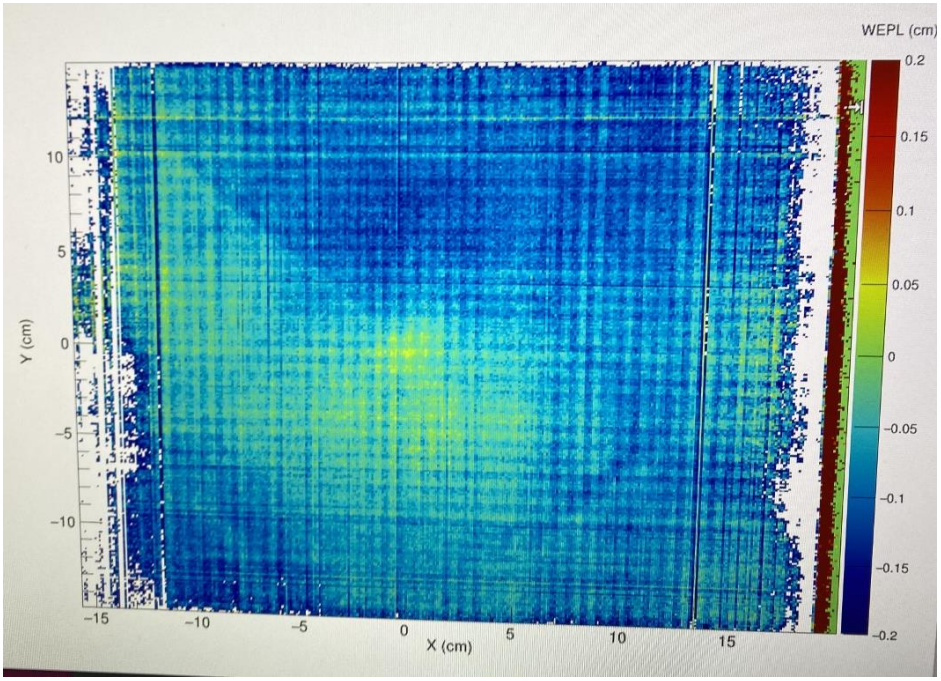

Fig. 19: Initial detector calibration map, showing WEPL values across all channels, taken prior to pig head images.

An initial range detector calibration measurement was carried out as described in section 3.1.2 and shown above in Figure 19. A position calibration described in section 3.1.1 was similarly performed.

The x-ray images of the two subjects were taken to provide a control image of clinical quality for RSP, resolution, and dose comparison. Both images were taken on the Philips® Brilliance™ Big Bore 12-slice CT with vertical mount by P-Cure™. Images were taken at 120 kVp tube voltage, 440 mA tube current, and 0.625mm thick slices. Scan time was 30

seconds for each subject. Image reconstruction time was 1 minute from first signal received for each subject.

Proton CT images were constructed using images taken from the ProtonVDA phase II scanner in conjunction with NIU and Fermilab, discussed in detail in chapter 3. Ninety images were taken at four-degree increments on a calibrated rotating platform for each sample. The data were fed into a GEANT4 reconstruction algorithm using the iterative techniques discussed in chapter 2. Each beam delivery consisted of 2-3 million protons over a 30x30cm^2 field size delivered in under a second. Each 2D image took 3-4 seconds to construct the respective radiograph, while the platform turned to the next position. In total, the process took fifteen minutes, with one engineer driving the beamline on verbal command, one engineer turning the platform and ensuring the radiographs were finished compiling before moving on to the next image, and one engineer directing the process in real time and counting the images. With a fully integrated system, these roles would be automated and coincide on a single therapeutic operator. The radiograph datasets were then compiled and constructed via ProtonVDA's GEANT4 algorithm using the iterative reconstruction techniques discussed in section 2.3 by Ethan DeJohgh. These were output in raw image format, which was then converted to DICOM format via Dicompyler, as discussed in section 3.3.

4.2 Registration and comparison of images

The x-ray CT and proton CT images, both in DICOM format, were uploaded to Velocity, a radiographic image staging program, registered, then resampled to the same DICOM space to allow for direct comparisons of RSP. Great care was taken in the physical transferral of the two subjects between scanning sites so as to not cause disruptions in the soft tissue. Furthermore, all image studies were performed in a 45 minute timeframe so as to avoid any longer-term tissue settling. The resultant high-quality image fusions prove that this was done well, and did not cause discrepancy in the two setups. The x-ray images were fitted to the stochastic HU-RSP curve used clinically by NMPC, in order to directly compare the RSP of the two modalities. Figures 20-23 show ROI-specific comparisons of the pork tissue samples. Figures 24-26 show ROI-specific comparisons of the pig head samples. For the pork tissue sample, the axial direction is along the vertical axis of the bucket. For the pig head sample, the axial direction is along the axis from the top of the skull to the bottom of the jaw. For figures 20-26 below, the image enclosed within the yellow region is the pCT superimposed over the same area of the x-ray CT.

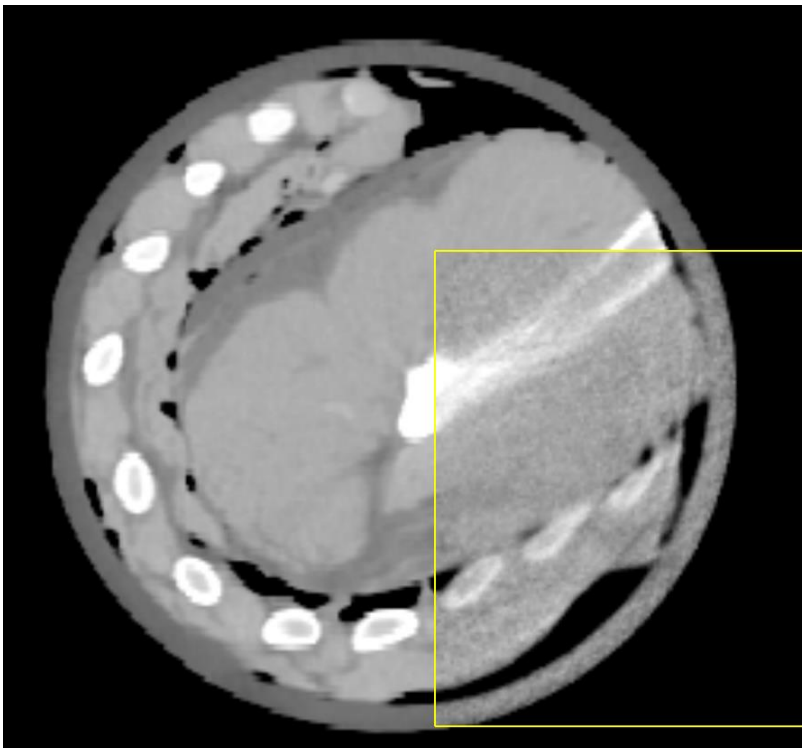

Fig. 20: Pork tissue axial image on a CT slice with high-Z material.

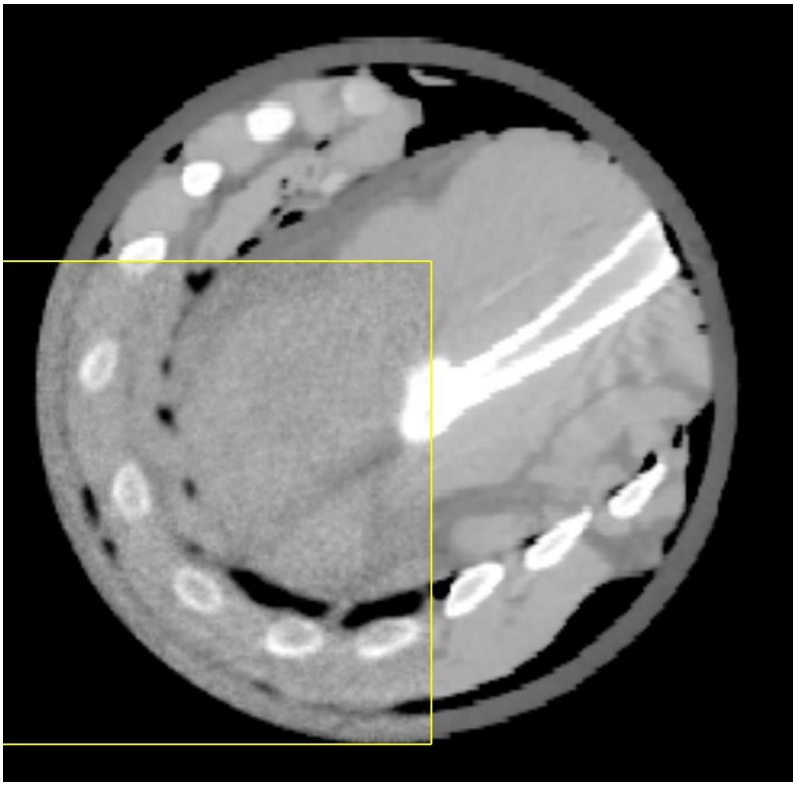

Fig. 21: The same axial slice as Figure 20, with the ROI on the other side.

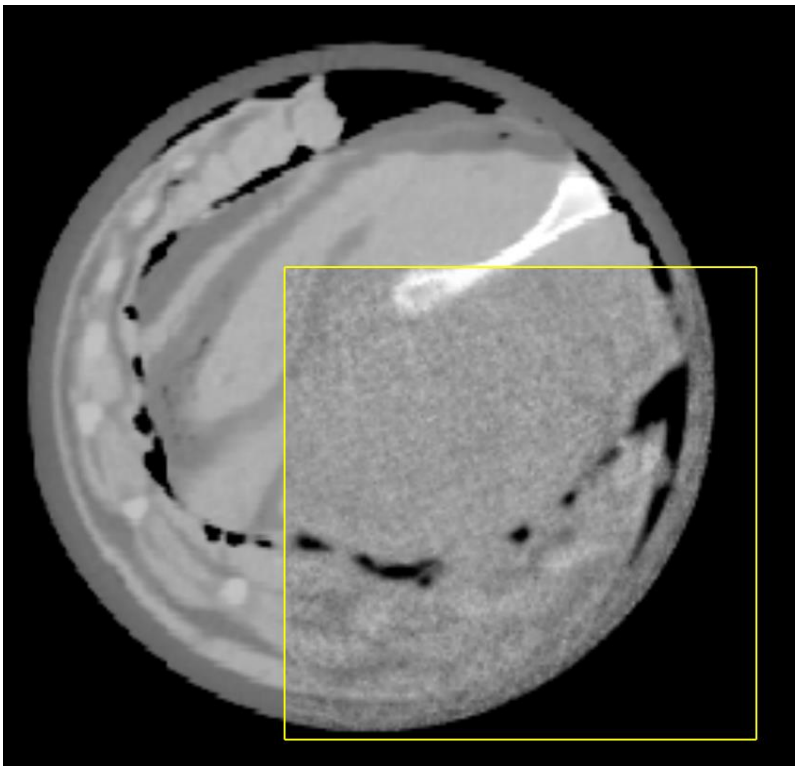

Fig. 22: Pork tissue axial image on a CT slice with high contrast in soft tissue separating muscle and fat.

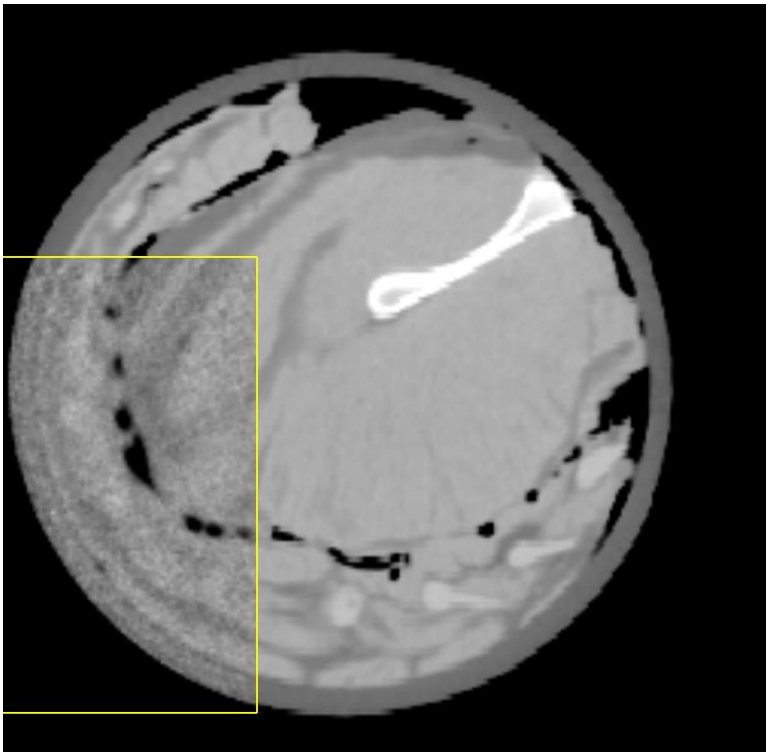

Fig. 23: The same axial slice as Figure 20, with the ROI on the other side.

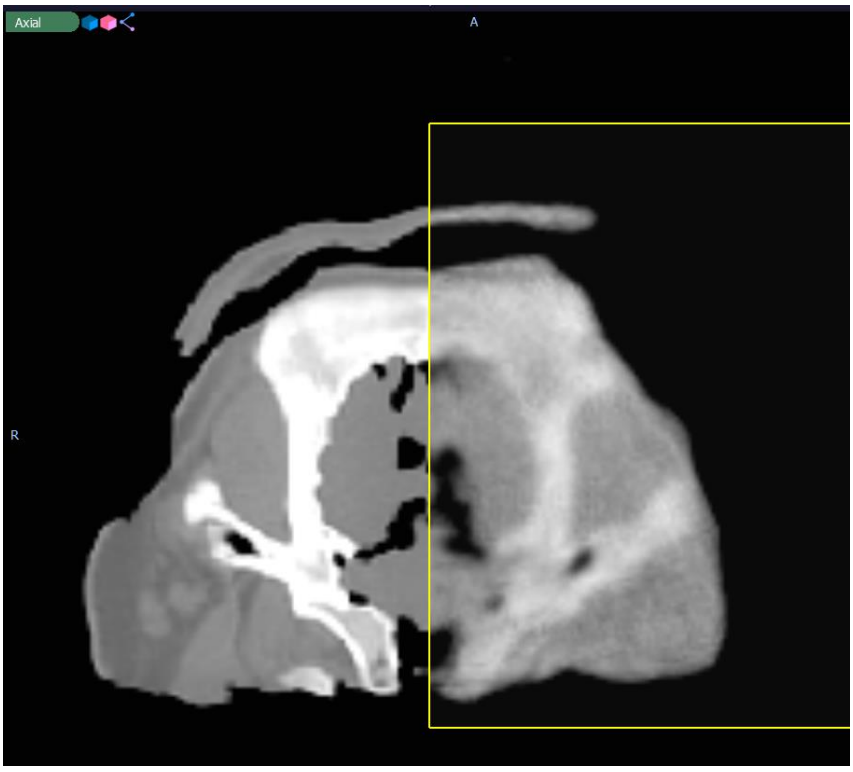

Fig. 24: Pig head axial image of a medial CT slice centered in the brain.

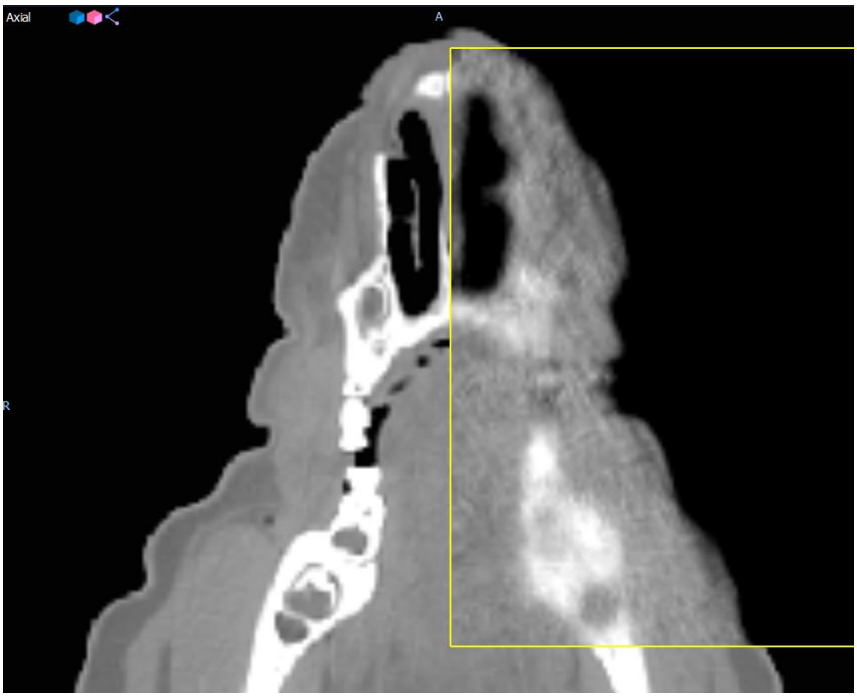

Fig. 25: Pig head axial image on a CT slice in the middle of the nose and jaw, showing sinuses as well as high-Z dental bone.

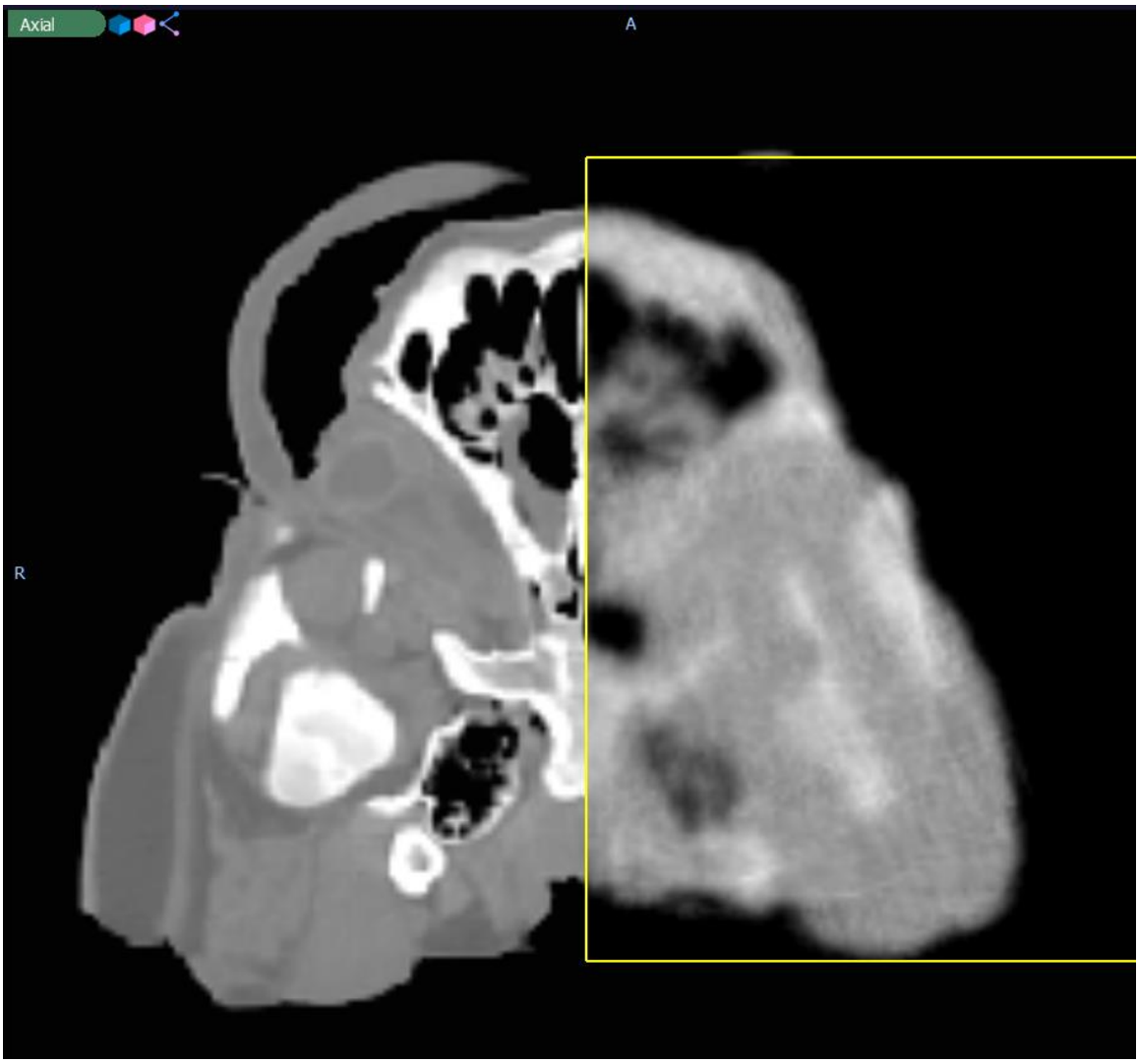

Fig. 26: Pig head axial image on a CT slice in the middle of the frontal sinuses. Sinus frontalis rostralis medialis, sinus frontalis rostralis lateralis, *and the superior aspect of the* labyrinthus ethmoidalis *can be seen here.*

4.3 Calculated RSP values

RSP for each region of interest across all scans is presented in Table 1 below. ROIs were selected based on tissue type as compared to distinct anatomical regions in order to provide comparison directly between the two targets. Screenshots of each individual ROI can be seen in Appendix A.

Table 1: Pig head RSP values for various sites.

		XCT			pCT			
Site	**volume (CC)**	**RSP**	**min**	**max**	**RSP**	**min**	**max**	**% difference**
bone	119.31	**1.31**	0.20	1.69	**1.24**	0.23	0.76	**-5.38%**
brain	70.79	**1.03**	0.08	1.16	**1.01**	0.09	0.95	**-1.77%**
fat medial	0.62	**0.97**	0.95	0.99	**1.00**	0.95	0.92	**2.82%**
fat peripheral	6.95	**0.95**	0.92	0.98	**0.96**	0.92	1.00	**0.49%**
muscle medial	10.71	**1.04**	1.00	1.08	**1.04**	1.00	1.02	**0.10%**
muscle peripheral	10.06	**1.05**	1.02	1.09	**1.06**	1.02	0.43	**0.67%**

Table 2: Pork shoulder and ribs RSP values for various sites.

		XCT			pCT			
Site	**volume (CC)**	**RSP**	**min**	**max**	**RSP**	**min**	**max**	**% difference**
Bone hard	113.09	**1.28**	1.09	1.72	**1.22**	0.84	1.61	**-4.68%**
Bone soft	5.66	**1.10**	1.07	1.12	**1.12**	0.79	1.31	**2.50%**
Fat medial	15.86	**1.00**	0.93	1.04	**1.00**	0.90	1.10	**0.49%**
Fat peripheral	19.08	**0.98**	0.92	1.00	**0.99**	0.88	1.08	**0.82%**
Muscle medial	48.49	**1.05**	1.02	1.06	**1.04**	0.96	1.14	**-0.15%**
Muscle peripheral	21.61	**1.05**	1.00	1.07	**1.04**	0.93	1.14	**-0.40%**

4.4 Path length differences

To directly compare path length, the registered scans were imported into RayStation treatment planning system version 9A. Single spots were delivered into the target regions discussed in subsection 3.4. Line doses of each spot were compared, and measurement depths were recorded at the R80 of each spot. The dose calculation grid was set to 0.1cm, the finest setting available. Dose was calculated using a Monte

Carlo algorithm with 0.5% uncertainty. The setup and line dose of each spot can be seen in Appendix B. A cluster of seven spots, spaced in a hexagonal pattern 1cm apart, was additionally measured for the pig head sinus following concerns of lateral equilibrium through high-Z to low-Z boundaries as well as pockets of air.

Table 3: Pig head line dose comparisons for single spots, and a cluster of 7 spots additionally for the sinus.

Spot	Energy	R80 range difference on pCT scan
High-Z spot	150 MeV	3.42%
Low-Z spot	150 MeV	3.49%
Sinus spot (single)	100 MeV	-2.01%
Sinus spot (7 clustered)	100 MeV	1.66%

Table 4: Pork shoulder and ribs line dose comparisons for single spots.

Spot	Energy	R80 range difference on pCT scan
High-Z spot	150 MeV	0.12%
Low-Z spot	150 MeV	-0.06%

CHAPTER 5 - DISCUSSION

Proton CT images taken in this study show generally good agreement between x-ray derived RSP and pCT RSP. Variances in hard and soft tissue are clearly delineated, though variances in types of soft tissue are more difficult to identify on pCT. It is likely that the 2.8% RSP difference for medial fatty tissue is due to the necessarily small size of the ROI selected. Hard and soft bone was more difficult to determine distinct boundaries compared to x-ray CT, and showed the greatest variance in RSP between the image modalities. This could also be attributed to a fundamental inaccuracy in the x-ray HU-to-RSP conversion curve. Before considering this further, one must first tackle the issue of identifying a "ground truth".

The philosophical issue of identifying a "ground truth" is a difficult one in this comparative study. It is impossible for x-ray images to measure RSP directly without the aid of a conversion curve. Proton imaging is only capable of measuring RSP directly. Thus, the proton images should theoretically be the ground truth. However, the ProtonVDA phase 2 imager is a prototype model. Proton imaging is a new and burgeoning field, while x-ray CT has over fifty years of development and technological advancement. As such, it is disingenuous to directly compare one as experimental and one as ground truth. Hence, the intent of this study was

put forward as a comparison of the two image modalities. It could be assumed, if it had the 50+ years of development that x-ray CT has enjoyed, that proton imaging would be of comparable quality to x-ray imaging. If this were the case, such a study would not be necessary. This work has, in part, demonstrated that proton imaging is well on its way to reaching the quality standard of x-ray imaging.

The path length analysis of delivered spots presents generally high range variance for pig head measurements as compared to pork shoulder sample measurements. This suggests that heterogeneity of the target plays a significant factor measured dose differences between the two scans. The path length difference between the sinus single spot and sinus hexagonal spot cluster also suggests that scattering conditions between the two scans are not modeled similarly. Future studies should aim to use more advanced pCT reconstruction algorithms to more accurately model scattering conditions.

The increased noise in the images and loss of spatial resolution of finer structures can be attributed to many things. Most notably, the dead time of the SSD positional detectors limiting the image rate to one million protons per second restricts the time that a full tomographic image can take to collect. This, in turn, limits the amount of signal that can be received to construct a high-quality image in order to keep imaging time to clinically acceptable parameters. Additional constraints on image

quality are primarily derived from the MLP calculation as well as the complex iterative reconstruction algorithm. This should be a major focus of future development into pCT imaging.

CHAPTER 6 - CONCLUSION AND FUTURE DIRECTIONS

This work presented a comparison of two complex animal tissue samples imaged via x-ray CT and proton CT. The x-ray scans were performed with a commercially available clinical x-ray CT scanner on a vertical mount. The proton CT scans were performed with ProtonVDA's Phase II prototypical proton radiography and CT scanner. The fundamental schematics of the scanner have been presented. X-ray and proton images were taken within minutes of each other in order to minimize tissue settling, fluid pooling, or other setup inconsistencies.

Future studies should aim to bridge this gap of identifying "ground truth". One way to approach this would be to produce radiographs and tomographs of complex, heterogeneous phantoms of many materials with known RSP values, such as an anatomically-accurate head phantom. Many studies with phantoms comprising materials of known RSP have been performed using this imager (3, 12). However, a complex phantom would allow a more accurate analysis of RSP at borders between tissue types, as well as test its ability to accurately delineate borders between tissues in heterogeneous regions. Future studies on organic tissue should focus on high-Z regions, as well as air-filled cavities such as the sinus and lung, as these showed the greatest variance between the two image modalities.

APPENDIX A: ROIs OF RSP MEASUREMENTS

Pork shoulder and ribs:

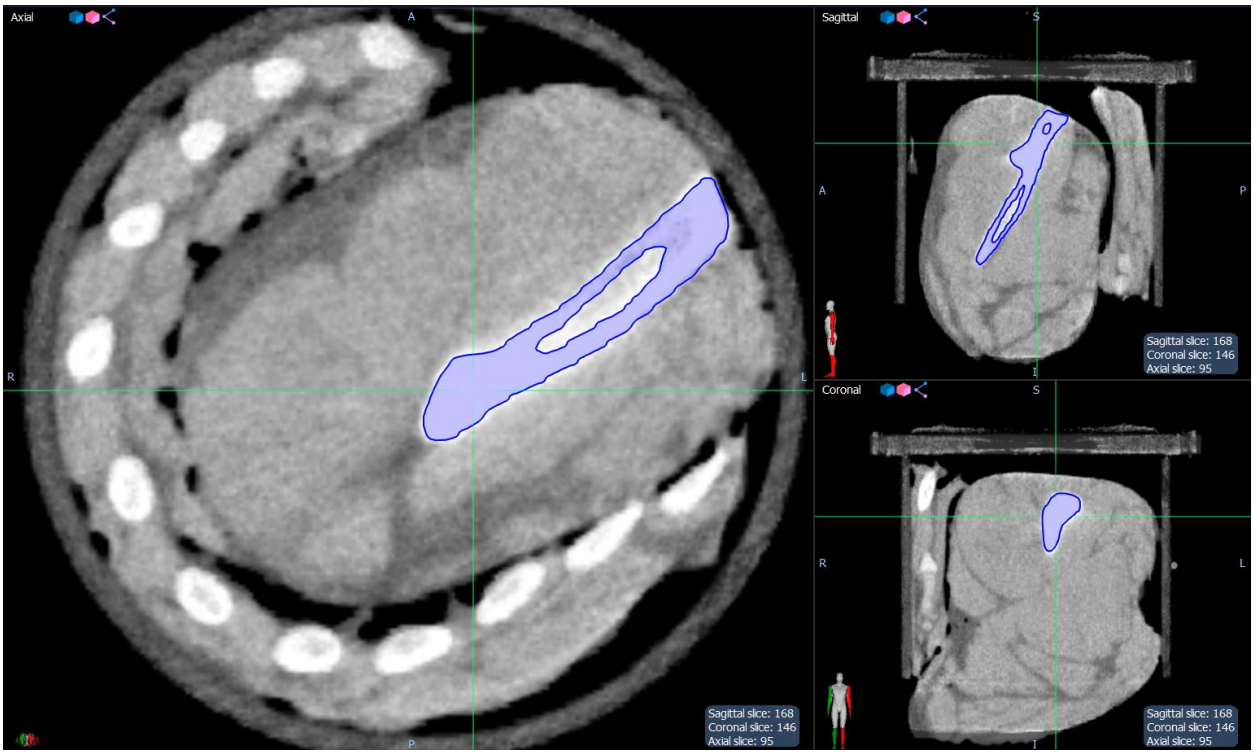

Fig. A1: Cortical bone ROI slice.

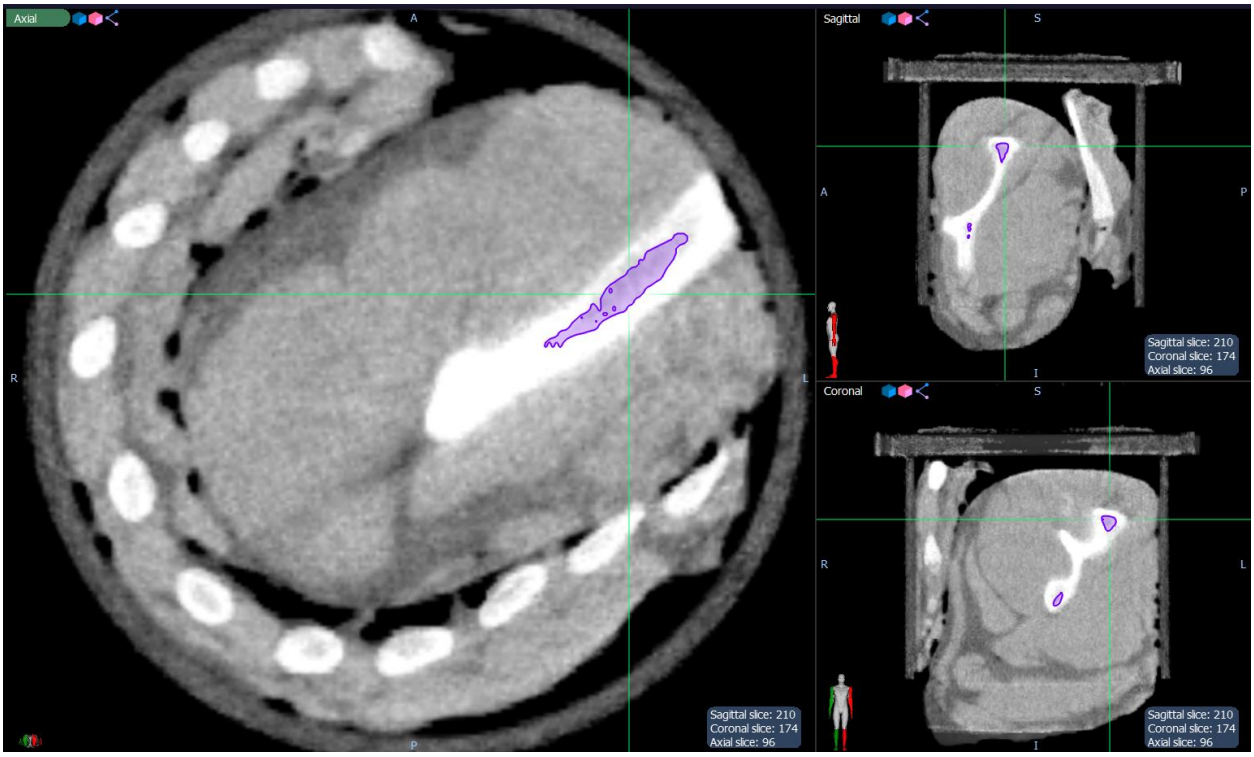

Fig. A2: Soft bone ROI slice.

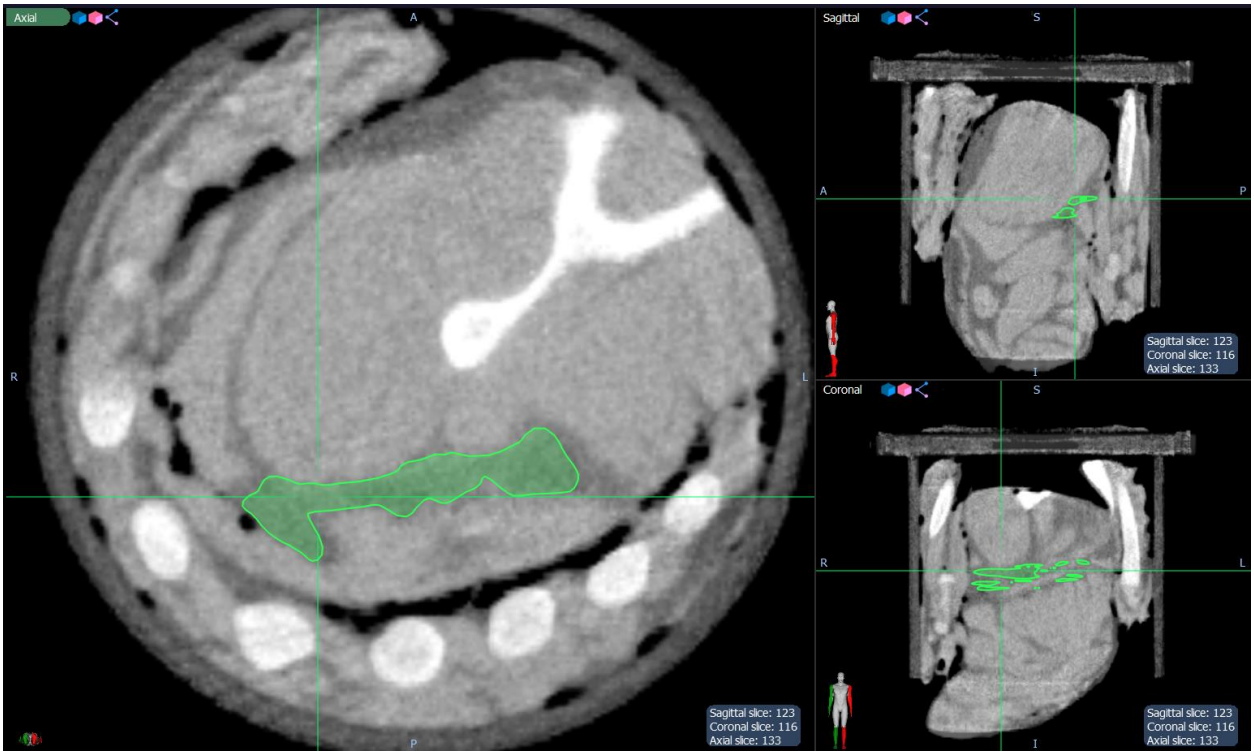

Fig. A3: Medial fatty tissue ROI slice.

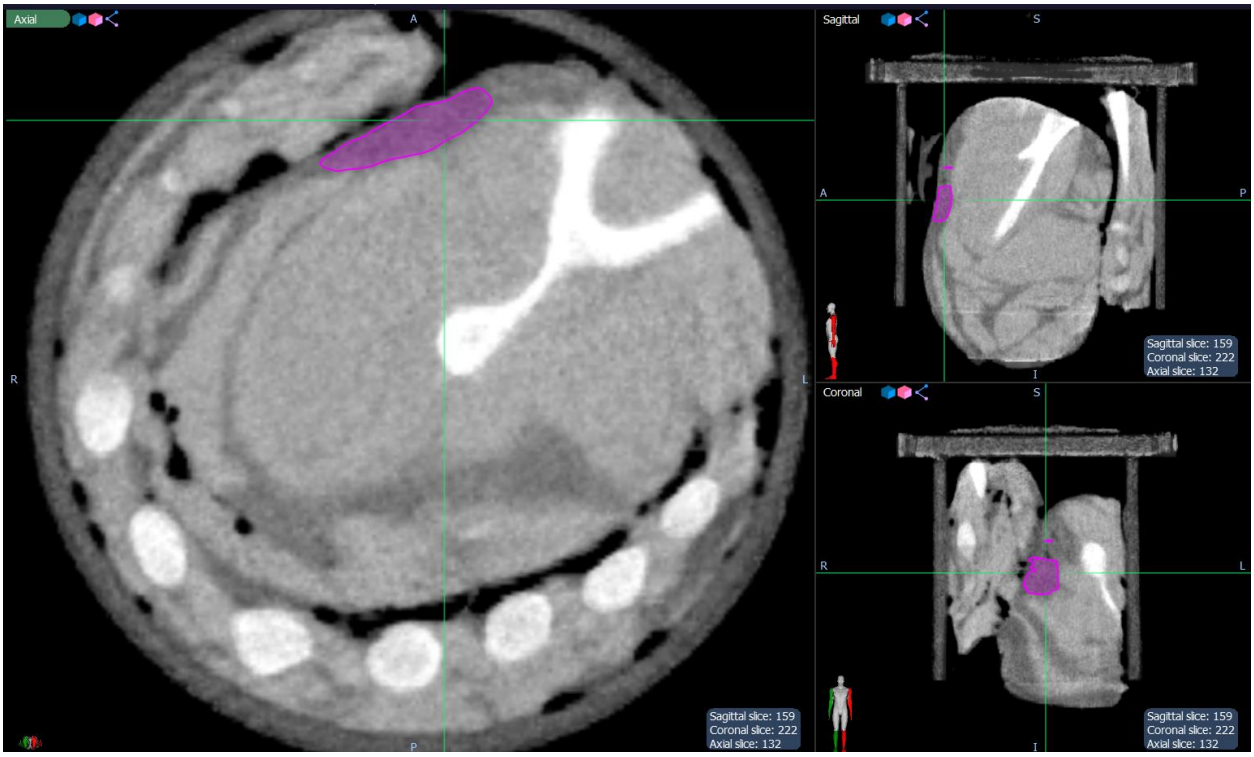

Fig. A4: Peripheral fatty tissue ROI slice.

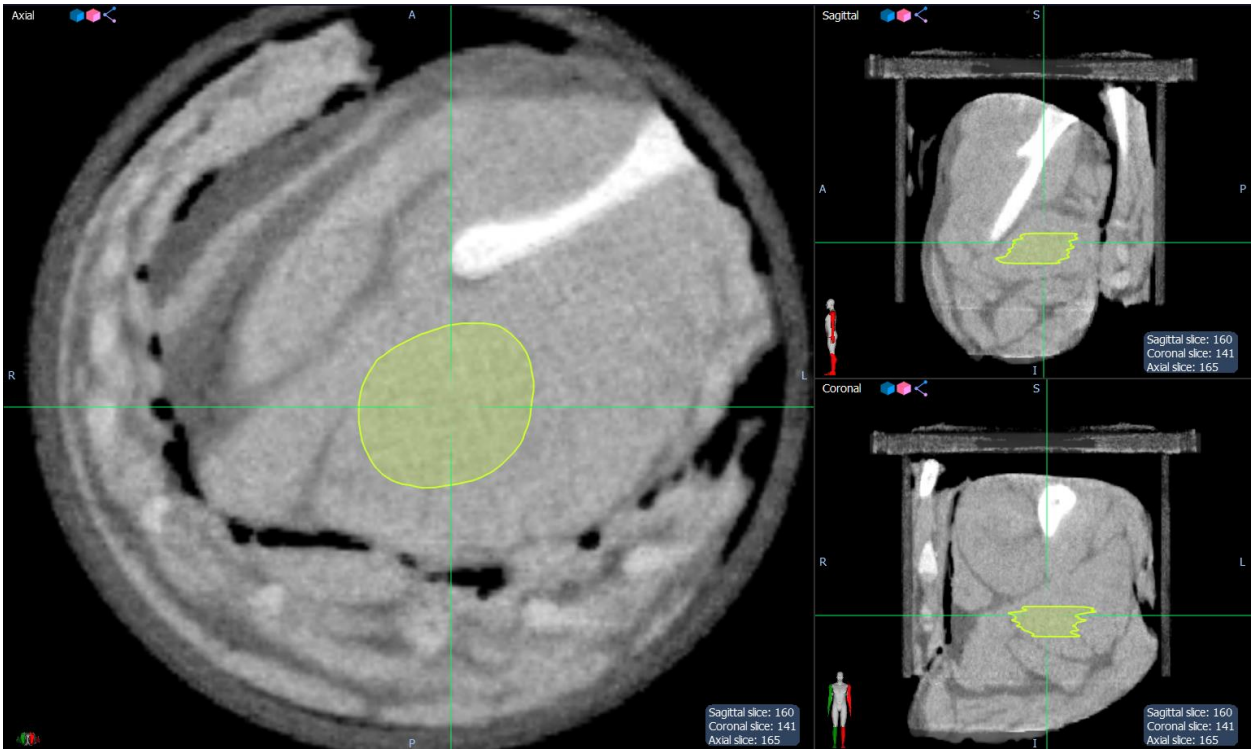

Fig. A5: Medial muscle ROI slice.

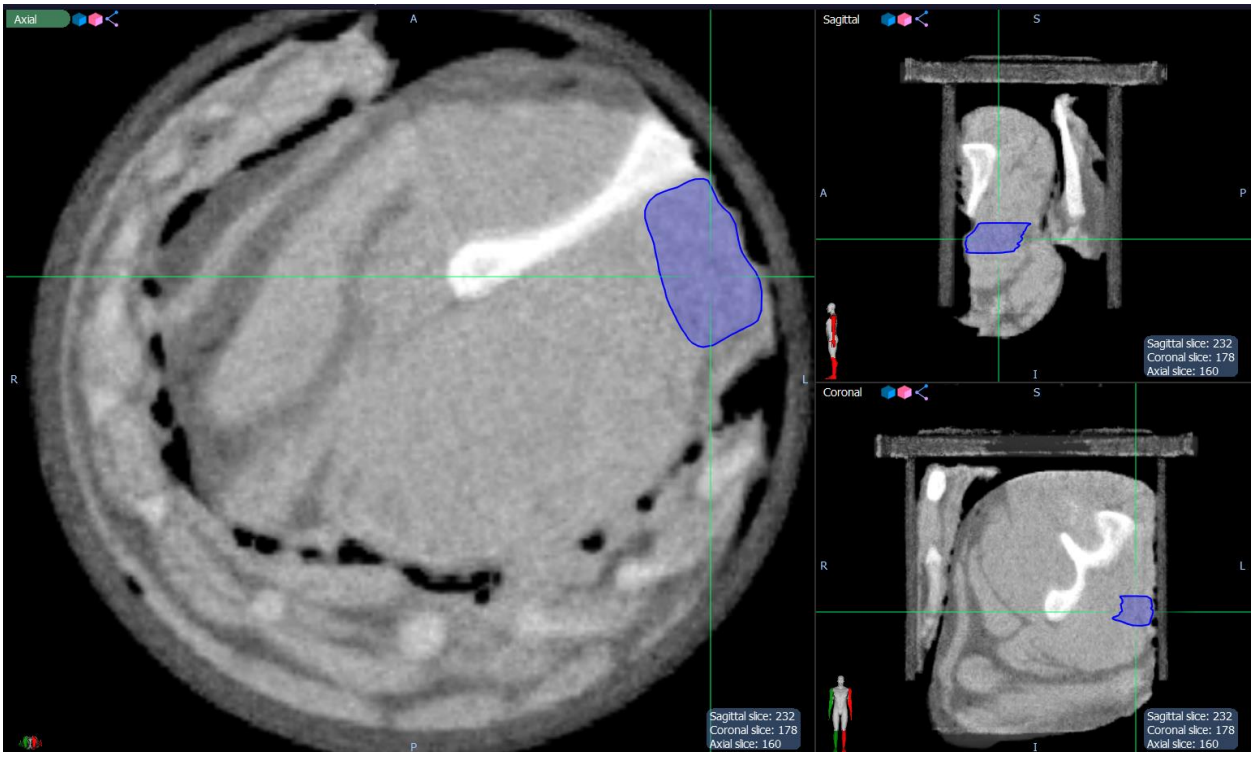

Fig. A6: Peripheral muscle ROI slice.

Pig head:

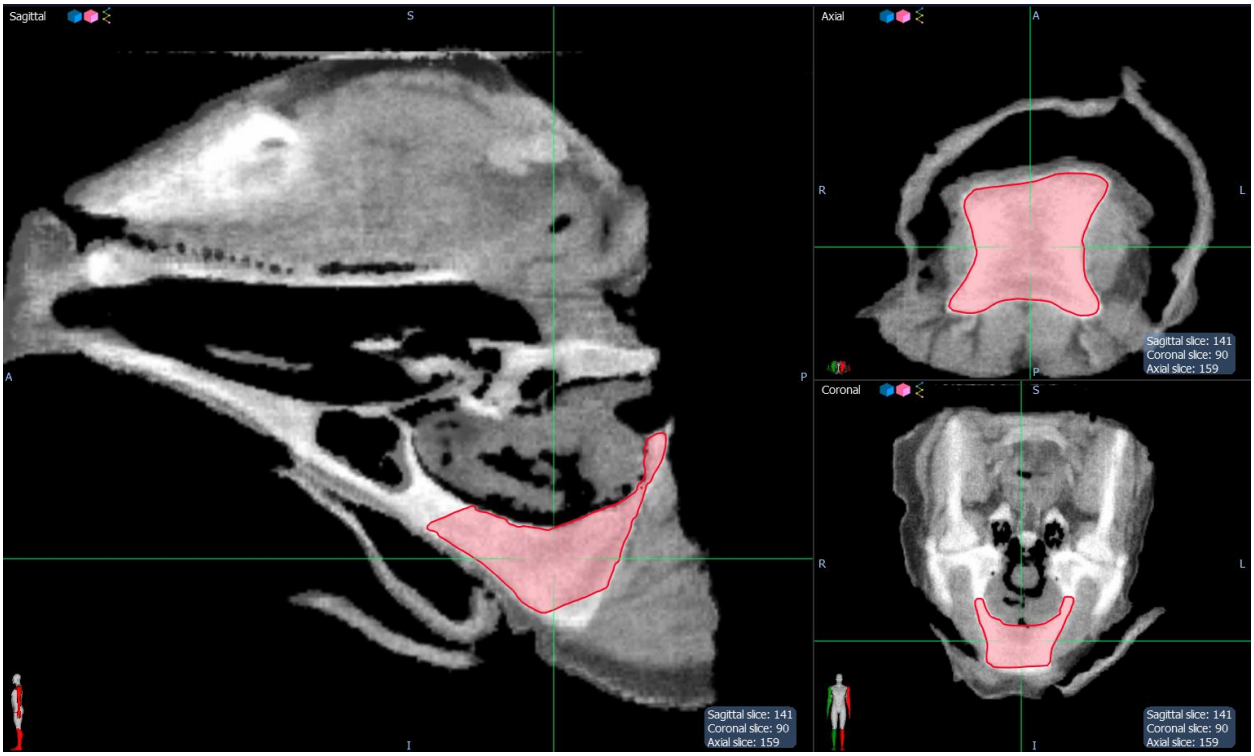

Fig. A7: Bone ROI slice.

Fig. A8: Brain ROI slice.

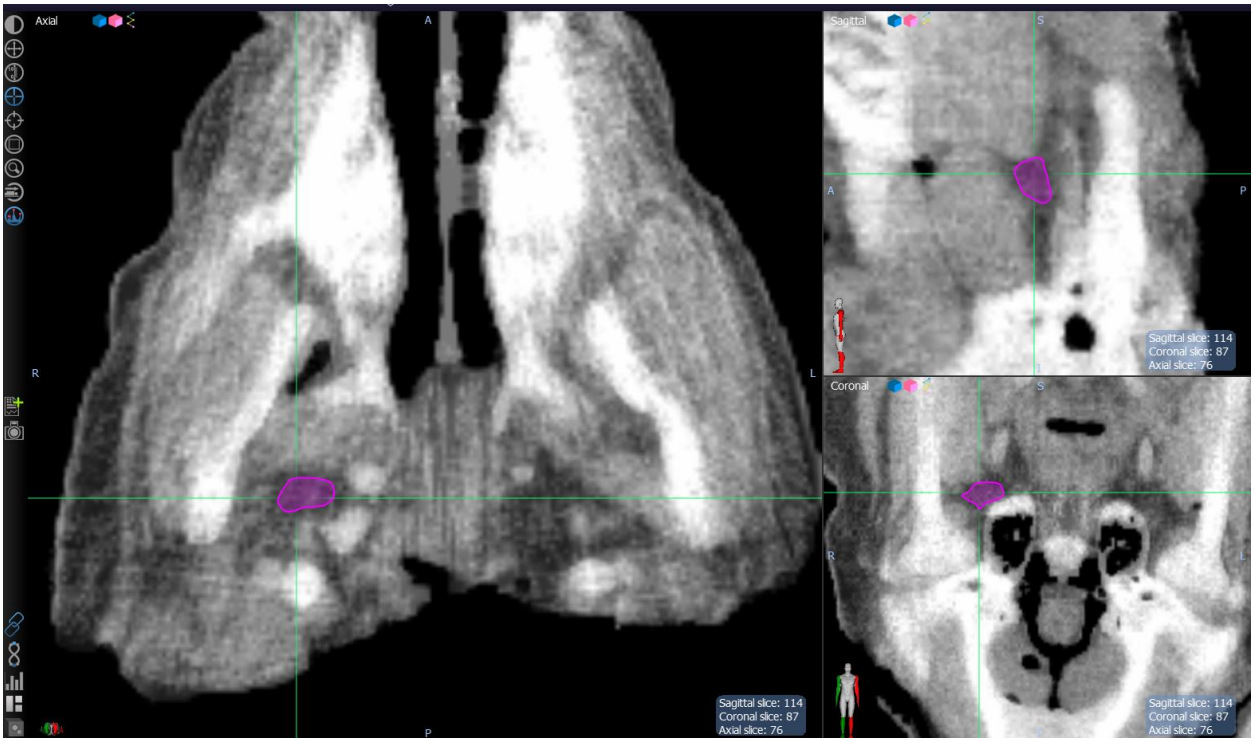

Fig. A9: Medial fatty tissue ROI slice.

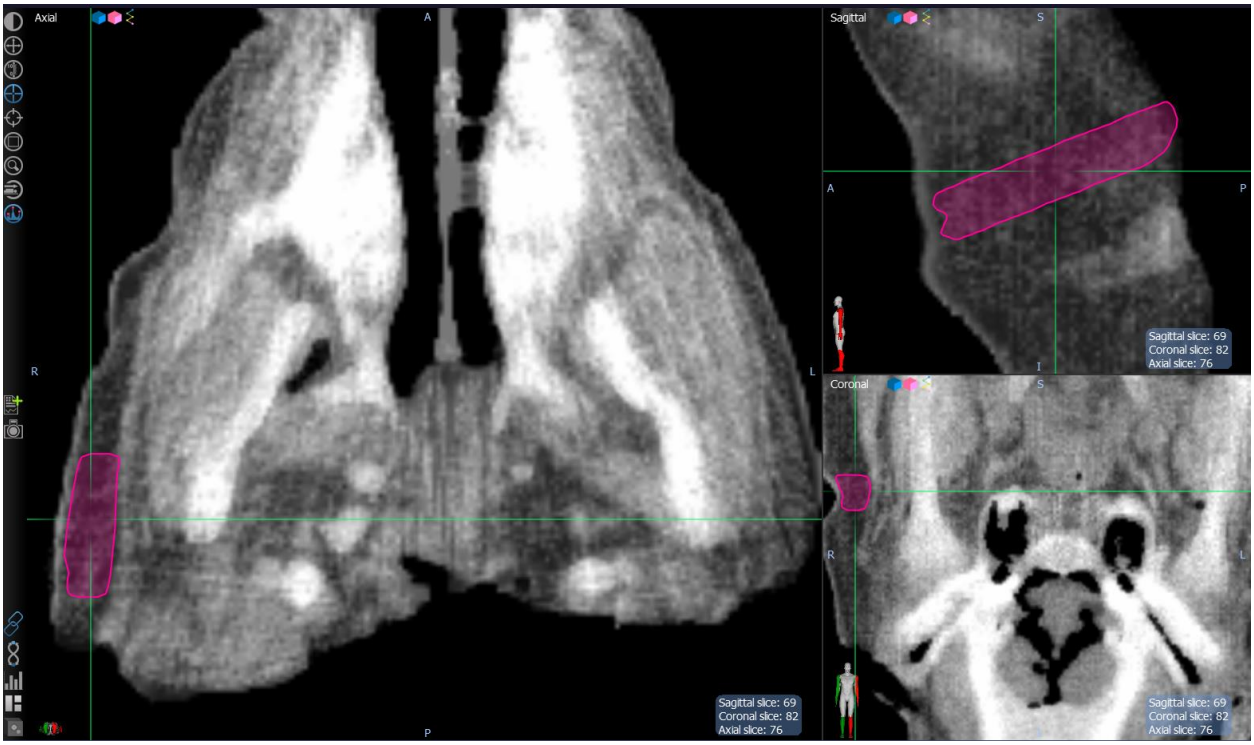

Fig. A10: Peripheral fatty tissue ROI slice.

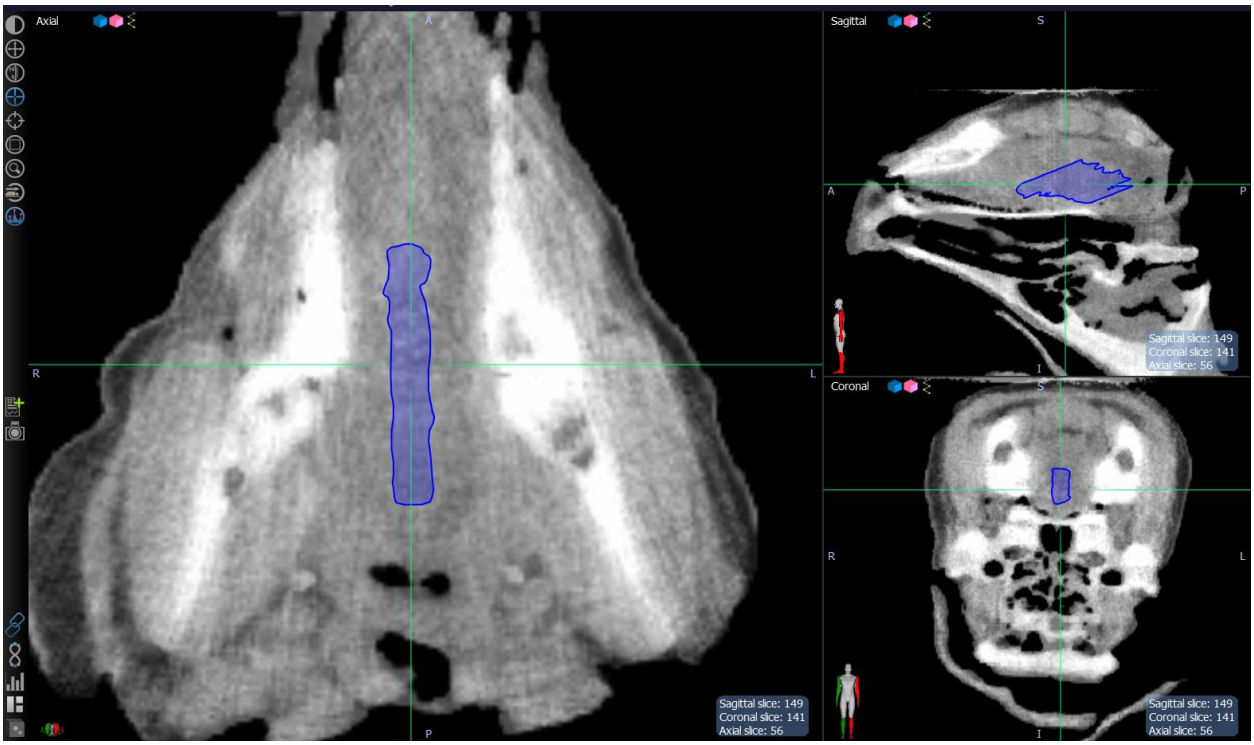

Fig. A11: Medial muscle ROI slice.

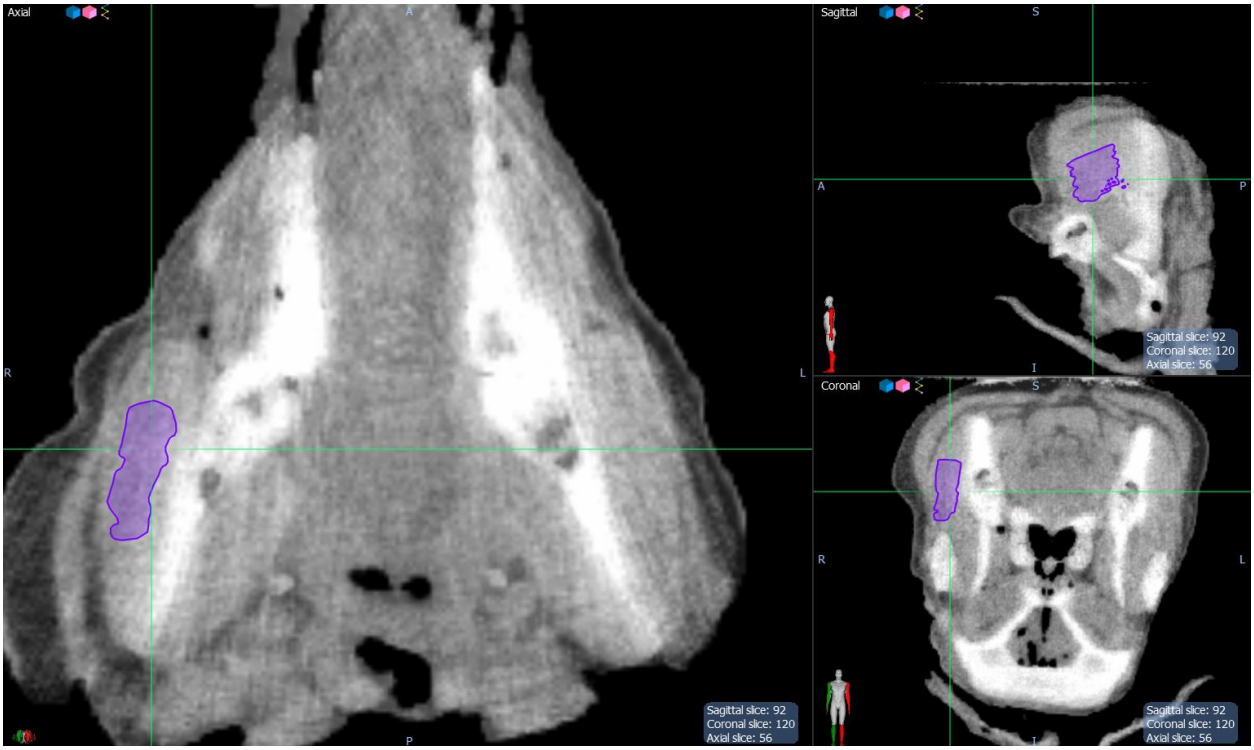

Fig. A12: Peripheral muscle ROI slice.

APPENDIX B: LINE DOSES OF INDIVIDUAL SPOTS

All images here follow the same format:

- Upper left window: xCT with spot.
- Lower left window: pCT with same spot.
- Upper right window: Line dose overlay.
- Lower right window: Subtraction isodose planes.

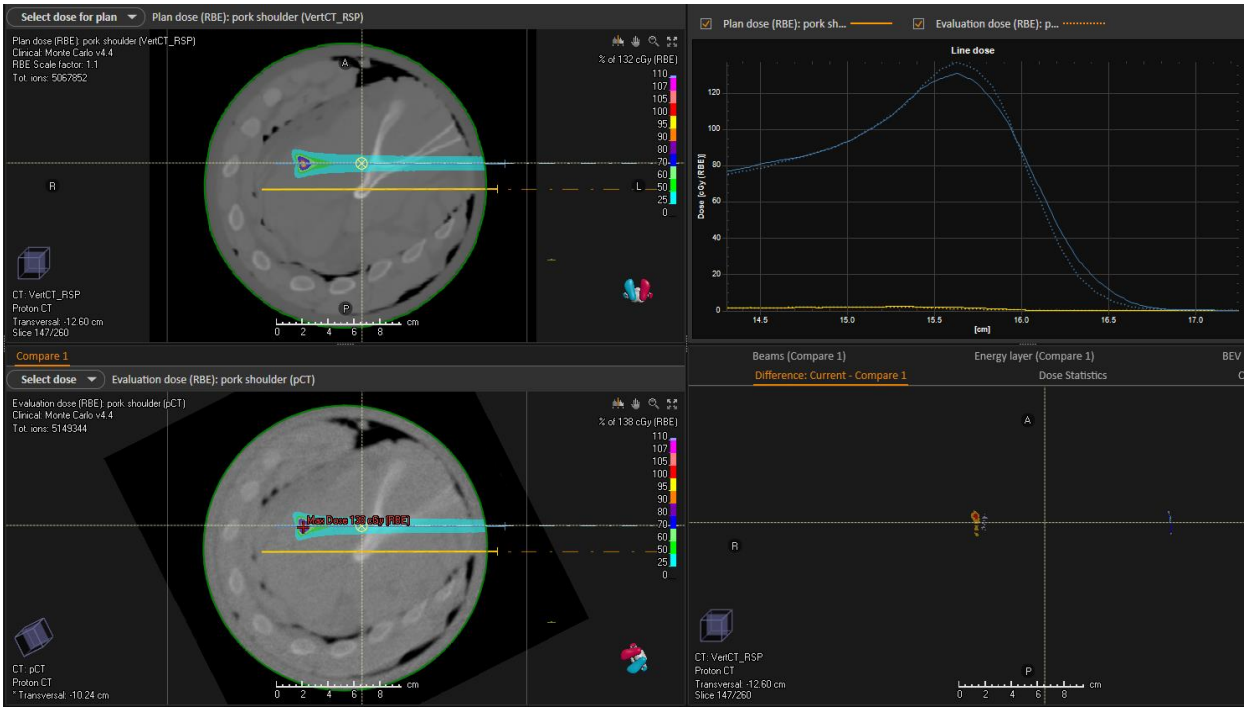

Fig. B1: Pork shoulder and ribs sample, high-Z spot.

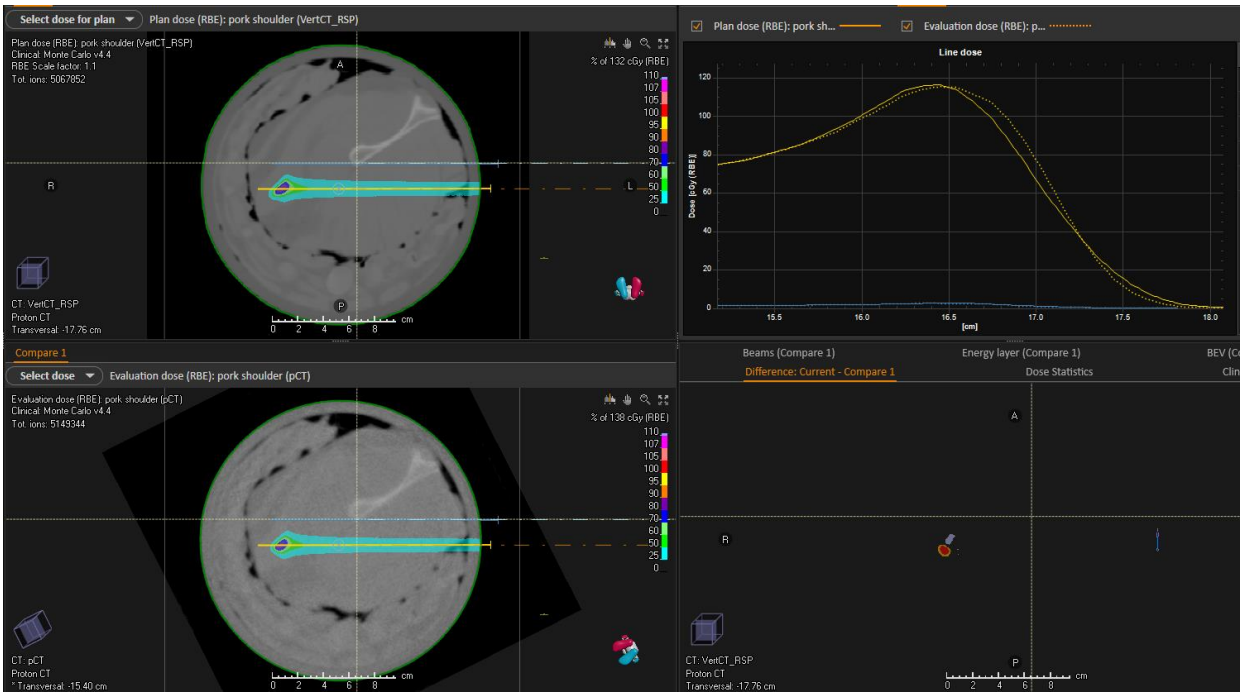

Fig. B2: Pork shoulder and ribs sample, low-Z spot.

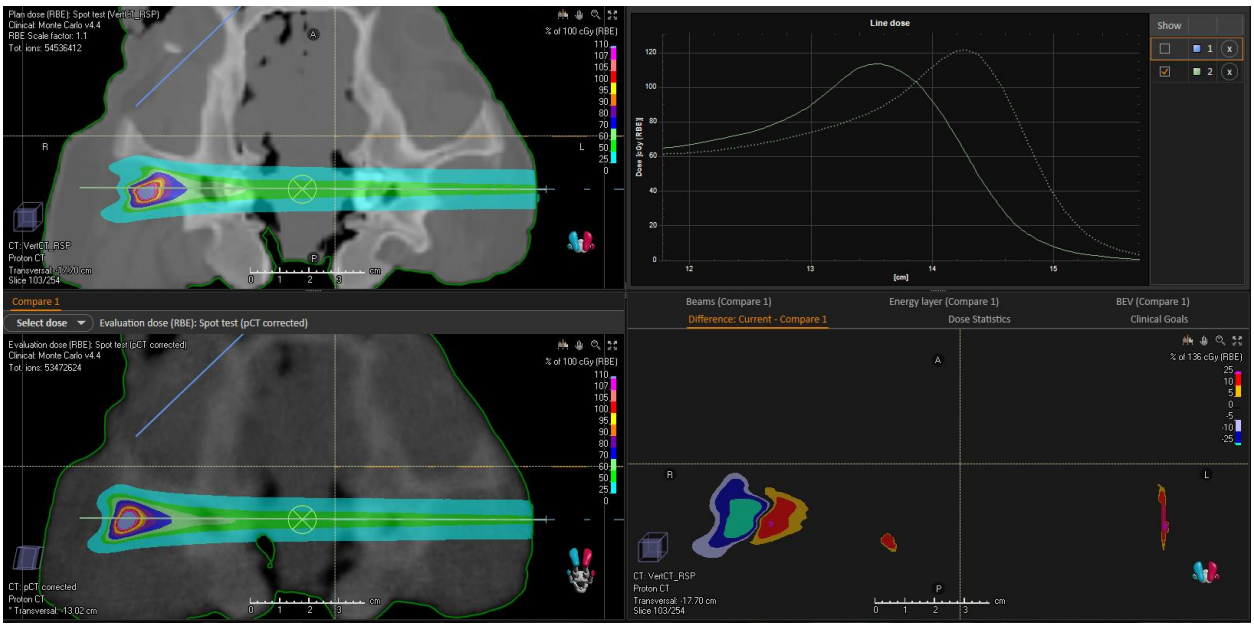

Fig. B3: Pig head sample, high-Z spot.

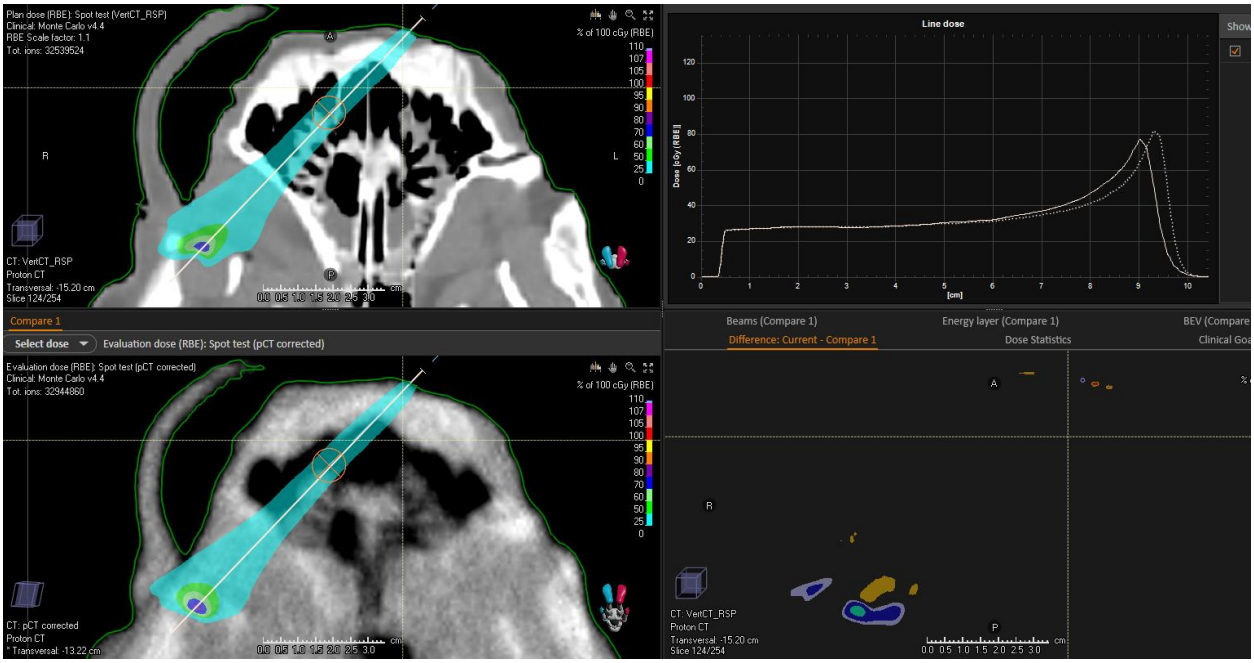

Fig. B4: Pig head sample, sinus spot array. Single spot analysis is the spot in the center of this array, measured separately.

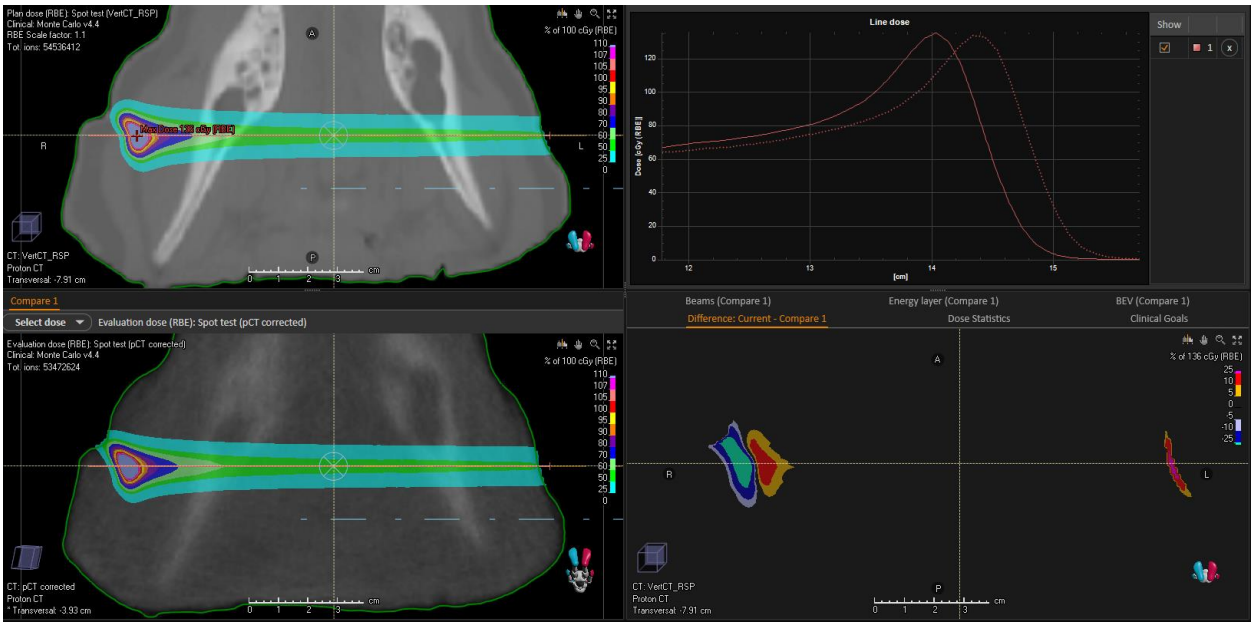

Fig. B5: Pig head sample, low-Z spot.

REFERENCES

1. **Wilson, Robert R.** "Radiological Use of Fast Protons." *Radiology*, vol. 47, no. 5, 1946, pp. 487–491., doi:10.1148/47.5.487.

2. "Introduction to Proton Beam Radiation Therapy." *Introduction to Proton Beam Radiation Therapy - Chang Gung Memorial Hospital*, www.chang-gung.com/en/news-1.aspx?rows=8&page=1&type=&id=352&mid=120&bid=3.

3. **Schulte, R., et al.** "Conceptual Design of a Proton Computed Tomography System for Applications in Proton Radiation Therapy." *IEEE Transactions on Nuclear Science*, vol. 51, no. 3, 2004, pp. 866–872., doi:10.1109/tns.2004.829392.

4. **Schuemann, J, et al.** "Site-Specific Range Uncertainties Caused by Dose Calculation Algorithms for Proton Therapy." *Physics in Medicine and Biology*, vol. 59, no. 15, 2014, pp. 4007–4031., doi:10.1088/0031-9155/59/15/4007.

5. **Schaffner, B, and E Pedroni.** "The Precision of Proton Range Calculations in Proton Radiotherapy Treatment Planning: Experimental Verification of the Relation between CT-HU and Proton Stopping Power." *Physics in Medicine and Biology*, vol. 43, no. 6, 1998, pp. 1579–1592., doi:10.1088/0031-9155/43/6/016.

6. **Paganetti, Harald.** "Range Uncertainties in Proton Therapy and the Role of Monte Carlo Simulations." *Physics in Medicine and Biology*, vol. 57, no. 11, 2012, doi:10.1088/0031-9155/57/11/r99.

7. **Bär, Esther, et al.** "The Potential of Dual-Energy CT to Reduce Proton Beam Range Uncertainties." *Medical Physics*, vol. 44, no. 6, 2017, pp. 2332–2344., doi:10.1002/mp.12215.

8. **Cormack, A. M.** "Representation of a Function by Its Line Integrals, with Some Radiological Applications." *Journal of Applied Physics*, vol. 34, no. 9, 1963, pp. 2722–2727., doi:10.1063/1.1729798.

9. **Gibbons, John P., and Faiz M. Khan.** Khan's the Physics of Radiation Therapy. Wolters Kluwer, 2020.

10. **Eyges, Leonard.** "Multiple Scattering with Energy Loss." *Physical Review*, vol. 74, no. 10, 1948, pp. 1534–1535., doi:10.1103/physrev.74.1534.

11. **Lynch, Gerald R., and Orin I. Dahl.** "Approximations to Multiple Coulomb Scattering." *Nuclear Instruments and Methods in Physics Research Section B: Beam Interactions with Materials and Atoms*, vol. 58, no. 1, 1991, pp. 6–10., doi:10.1016/0168-583x(91)95671-y.

12. **Ordoñez, Caesar E., et al.** "Fast in Situ Image Reconstruction for Proton Radiography." *Journal of Radiation Oncology*, vol. 8, no. 2, 2019, pp. 185–198., doi:10.1007/s13566-019-00387-x.

13. **Aharoni, Ron, and Yair Censor.** "Block-Iterative Projection Methods for Parallel Computation of Solutions to Convex Feasibility Problems." *Linear Algebra and Its Applications*, vol. 120, 1989, pp. 165–175., doi:10.1016/0024-3795(89)90375-3.

14. **Gordon, Dan, and Rachel Gordon.** "Component-Averaged Row Projections: A Robust, Block-Parallel Scheme for Sparse Linear Systems." *SIAM Journal on Scientific Computing*, vol. 27, no. 3, 2005, pp. 1092–1117., doi:10.1137/040609458.

15. **Goldman, L. W.** "Principles of CT and CT Technology." *Journal of Nuclear Medicine Technology*, vol. 35, no. 3, 2007, pp. 115–128., doi:10.2967/jnmt.107.042978.

16. **Kaczmarz, Stefan.** Angenäherte Auflösung von Systemen linearer Gleichungen. Bulletin International de l'Académie Polonaise des Sciences et des Lettres. 1937, Vol. A, 35, pp. 355-357.

17. **Gordon, Richard, et al.** "Algebraic Reconstruction Techniques (ART) for Three-Dimensional Electron Microscopy and X-Ray Photography." *Journal of Theoretical Biology*, vol. 29, no. 3, 1970, pp. 471–481., doi:10.1016/0022-5193(70)90109-8.

18. **Rai, Saroj.** "Image Quality Measures in Proton Computed Tomography." [Unpublished master's thesis.] *Northern Illinois University,* 2015.

19. **Smith, Alfred R.** "Vision 20/20: Proton Therapy." *Medical Physics*, vol. 36, no. 2, 2009, pp. 556–568., doi:10.1118/1.3058485.

20. **Wang, Dongxu, et al.** "On Proton CT Reconstruction Using MVCT-Converted Virtual Proton Projections." *Medical Physics*, vol. 39, no. 6Part1, 2012, pp. 2997–3008., doi:10.1118/1.4711752.

21. **Jin, Xin, et al.** "Anisotropic Total Variation for Limited-Angle CT Reconstruction." *IEEE Nuclear Science Symposuim & Medical Imaging Conference*, 2010, doi:10.1109/nssmic.2010.5874180.

22. **De Jongh, F., et al.** "Image Reconstruction with a Fast Monolithic Proton Radiography System." *PTCOG-2017 Proceedings,* 2017. Volume 99, Number 25, Supplement 2017.

23. **Johnson, Robert, et al.** "A Fast Experimental Scanner for Proton CT: Technical Performance and First Experience with Phantom Scans". *IEEE Trans Nucl Sci. 2016* February ; 63(1): 52–60. doi:10.1109/TNS.2015.2491918.

24. **Levenberg, Kenneth.** "A Method for the Solution of Certain Non-Linear Problems in Least Squares." *Quarterly of Applied Mathematics*, vol. 2, no. 2, 1944, pp. 164–168., doi:10.1090/qam/10666.

25. **Johnson, R.P., et al.** "Results from a Prototype Proton-CT Head Scanner." Conference on the Application of Accelerators in Research and Industry, CAARI 2016, 30 October – 4 November 2016, Ft. Worth, TX, USA.

26. **Welsh, J.S., et al.** "Image Reconstruction with a Fast, Monolithic Proton Radiography System." *International Journal of Radiation Oncology*Biology*Physics*, vol. 99, no. 2, 2017, doi:10.1016/j.ijrobp.2017.06.2376.

27. **Miller, Chelsea, et al.** "Reconstructed and Real Proton Radiographs for Image-Guidance in Proton Beam Therapy." *Journal of Radiation Oncology*, vol. 8, no. 1, 2019, pp. 97–101., doi:10.1007/s13566-019-00376-0.